

Deep Learning Pose Estimation for Multi-Label Recognition of Combined Hyperkinetic Movement Disorders

Laura Cif ^{1, 2}, Diane Demailly ^{2, 3}, Gabriella A. Horvàth ⁴, Juan Dario Ortigoza Escobar ^{5, 6, 7}, Nathalie Dorison ⁸, Mayté Castro Jiménez ¹, Cécile A. Hubsch ¹, Thomas Wirth ^{9, 10, 11}, Gun-Marie Hariz ¹², Sophie Huby ¹³, Morgan Dornadic ¹³, Zohra Souei ^{2, 14}, Muhammad Mushhood Ur Rehman ¹⁵, Simone Hemm ¹⁶, Mehdi Boulaymen ², Eduardo M. Moraud ^{17, 18}, Jocelyne Bloch ^{18, 19}, Xavier Vasques ²

¹ Service of Neurology, Department of Clinical Neurosciences, Lausanne University Hospital (CHUV) and University of Lausanne (UNIL), Lausanne, Switzerland

² Institut du Neurone, Montferrier sur Lez, France

³ Department of Neurology, Clinique Beau Soleil, Institut Mutualiste Montpelliérain, Montpellier, France

⁴ Department of Pediatrics, British Columbia Children's Hospital, Vancouver, British Columbia, Canada

⁵ Movement Disorders Unit, Pediatric Neurology Department, Institut de Recerca, Hospital Sant Joan de Déu, Barcelona, Spain

⁶ European Reference Network for Rare Neurological Diseases (ERN-RND), Barcelona, Spain

⁷ U-703 Centre for Biomedical Research on Rare Diseases (CIBER-ER), Instituto de Salud Carlos III, Barcelona, Spain

⁸ Pediatric Neurosurgery Department, CCMR Neurogenetique, European Reference Network Brainteam Member, Rothschild Foundation Hospital, Paris, France

⁹ Department of Neurology, University Hospital of Strasbourg, Strasbourg, France

¹⁰ Strasbourg Neuroscience Institute, Strasbourg University, Strasbourg, France

¹¹ Institute of Genetics and Cellular and Molecular Biology, INSERM-U964, CNRS-UMR7104, University of Strasbourg, Illkirch-Graffenstaden, France

¹² Department of Clinical Neuroscience, Umeå University, Umeå, Sweden

¹³ Department of Neurology, CHU Montpellier, Montpellier, France

¹⁴ Department of Neurosurgery, Fattouma Bourguiba University Hospital, Tunisia

¹⁵ University of Edinburgh, Scotland

¹⁶ Institute for Medical Engineering and Medical Informatics, School of Life Sciences, University of Applied Sciences and Arts Northwestern Switzerland, Muttenz, Switzerland

¹⁷ Department of Clinical Neurosciences, University Hospital Lausanne (CHUV), Lausanne, Switzerland

¹⁸ Defitech Center for Interventional Neurotherapies (NeuroRestore), University Hospital Lausanne and Ecole Polytechnique Fédérale de Lausanne, Lausanne, Switzerland

¹⁹ Department of Neurosurgery, Lausanne University Hospital (CHUV) and University of Lausanne (UNIL), Lausanne, Switzerland.

Abstract

Hyperkinetic movement disorders (HMDs) such as dystonia, tremor, chorea, myoclonus, and tics are disabling motor manifestations across childhood and adulthood. Their fluctuating, intermittent, and frequently co-occurring expressions hinder clinical recognition and longitudinal monitoring, which remain largely subjective and vulnerable to inter-rater variability. Objective and scalable methods to distinguish overlapping HMD phenotypes from routine clinical videos are still lacking. Here, we developed a pose-based machine-learning framework that converts standard outpatient videos into anatomically meaningful keypoint time series and computes kinematic descriptors spanning statistical, temporal, spectral, and higher-order irregularity/complexity features. In a screening-oriented window-level setting contrasting symptom-expressing segments against normative control movement, window-level performance was phenotype-dependent (e.g., dystonia $F1_1 = 0.84\text{--}0.89$, chorea $F1_1 = 0.81\text{--}0.96$, tremor $F1_1 \approx 0.82\text{--}0.83$), whereas aggregation of repeated 10-s observations improved patient identification and yielded highly conservative behavior in controls. For patient-level multi-label phenotyping, we harmonized expert annotations into a consensus reference, pooled window probabilities within subjects using robust percentile aggregation (p90), and applied label-wise thresholds tuned on training subjects under a control-aware operating regime. This achieved strong patient-level discrimination (macro-AUPRC 0.821 ± 0.019 ; macro-AUC 0.830 ± 0.029) and robust full-profile accuracy (best Hamming accuracy 0.764 ± 0.041 across cross-validation folds). Using best per-label patient-level models, error decomposition across 200 patient-label decisions (25 subjects \times 8 labels) yielded 28 total errors (86.0% correct), with near-ceiling performance for distinctive phenotypes (e.g., tics TP=3, TN=22; dystonia TP=20 with one FN and one FP). Decision-level permutation importance further showed that patient-level calls rely primarily on displacement-based evidence, with selective contributions from rhythmicity and higher-order irregularity/complexity descriptors and anatomically plausible regional patterns. Together, these results support scalable and explainable video-based phenotyping of co-occurring HMDs from routine recordings and motivate multicenter deployment and uncertainty-aware labeling for clinical translation.

1 Introduction

In both, adult and pediatric neurology, movement disorders (MDs) are broadly classified from a phenomenological perspective as either hyperkinetic (HMDs, characterized by excessive movements) or hypokinetic (hMDs, characterized by paucity and slowness of voluntary movements). Accurate, updated epidemiological data on MDs help to raise awareness, improve recognition, and facilitate timely diagnosis and treatment that remains especially symptomatic ¹. Despite the progress achieved for their clinical characterization and genetic diagnostic ^{2,3,4}, the recognition of MDs phenomenology remains challenging during clinical examination with disagreement even between MDs specialists, particularly for the complex presentations of many neurodevelopmental, neurodegenerative and monogenic disorders. The current classification of genetic MDs distinguishes between isolated, combined, and mixed categories ⁵.

Traditionally, clinicians identify HMDs through direct observation and assess them by using standardized clinical rating scales that usually focus on individual motor phenomena (e.g., scales for dystonia, tremor or tics). Despite their widespread use, they may not capture the full spectrum of motor phenomenology for each patient ^{6,7} and have inherent limitations, notably inter-rater variability, limited reproducibility, and the need for specialized training and expertise ⁸. Additionally, some scales focus on specific diseases ⁹ without potential for generalization or application to other conditions. By contrast, other scales ¹⁰ may have broader applicability to other developmental disorders. Currently, no available composite assessment tools enable the simultaneous identification and monitoring of MDs over different diseases associating HMDs and through lifespan, in both children and adults. Accurate and objective assessment of HMD, such as dystonia, tremor, chorea, myoclonus, or tics, is critical not only for diagnosis, but also for monitoring, facilitating effective patient care, and the development of targeted, symptom-specific interventions ¹¹.

Within artificial intelligence (AI), machine learning (ML) empowers computers to learn from data and improve learning performance over time without explicit programming¹². Deep learning (DL), a key subset of ML employs multi-layered neural networks to model complex patterns, and has proven effective in domains such as image and speech recognition. Recent advances in computer vision have demonstrated significant potential for the automated analysis of movements and provide objective measures of neurological signs based solely on noninvasive video footage, an easy-to-use alternative to laboratory-based motion analysis ^{8,13, 14}. Computer vision extends traditional object detection by using convolutional neural networks (CNNs) that model the topological relationships between key human joints ¹⁵. DL architectures ¹⁶ such as YOLO (You Only Look Once) demonstrate remarkable accuracy and efficiency in extracting human body landmarks from videos in real time ¹⁷; they generate rich spatiotemporal data, enabling the automatic differentiation of pathological from physiological movement patterns ¹⁸⁻²¹. Research leveraging DL for pose estimation has shown progress in various clinical applications, including gait analysis, rehabilitation assessment ⁸, tic detection and tremor quantification²², thereby facilitating more accurate, detailed and objective assessment and quantification of HMD ²³ compared to human observers.

Despite various developments, existing ML approaches for detecting HMD remain limited in scope, focusing on binary classification of individual HMD and frequently restricted to short, task-specific video segments ⁸. While most existing ML models for MD analysis rely on shallow feature representations, primarily using raw joint coordinates or velocity, they often fail to capture the temporal complexity and variability inherent to a pathological, involuntary movement ²⁴⁻²⁹. One unmet need remains the identification and quantification of combined MDs, both in neurology outpatient clinics and through remote assessments, to support disease monitoring and therapeutic decision-making. The field prospect is to extend DL developments for enhanced accuracy of phenotype classification, the cornerstone of both the diagnostic and treatment process ³⁰

We developed a pipeline that combines YOLOv8-based 2D pose estimation with clinically grounded time-series feature extraction and supervised classifiers to detect and classify multiple HMDs across diverse syndromic presentations using standard clinical videos. We specifically designed the evaluation to reflect realistic clinical operating regimes: a screening-oriented window-level setting contrasting symptom-expressing segments with normative control movement, and patient-level inference obtained by aggregating repeated short observations into consolidated phenotype calls. For multi-label detection, we harmonized annotations into a consensus reference and derived patient-level multi-label profiles from window probabilities using percentile pooling (p90) followed by label-wise thresholding tuned on training subjects under control-aware constraints, enabling phenotype-specific operating points aligned with different clinical priorities.

By applying this framework, we parallel a novel composite clinical tool designed to identify and quantify HMDs and associated motor features, after the age of achievement of the major motor developmental milestones, across the lifespan. We hypothesize that the hyperkinetic phenotypes captured by the Combined Dystonia Scale for Assessment of the Motor Phenotype (CODY-SAMP) can be accurately detected and their combinations automatically recognized from pose-derived features extracted from routine videos. Therefore, our aims were to (i) quantify window-level detection and subject identification for individual HMD phenotypes indexed by CODY-SAMP, (ii) enable clinically interpretable patient-level multi-label recognition of co-occurring HMDs phenomenology under control-aware operating regimes, (iii) benchmark model families and operating points to characterize trade-offs across clinical priorities, and (iv) link decisions to kinematic families and anatomical regions through decision-level feature-importance analyses. Progressively increasing clinical complexity, we address individual HMD detection, concurrent multi-label classification across standardized examination conditions.

2 Materials and Methods

2.1 Participant Recruitment and Video Acquisition

Twenty-one consecutive patients (range 17 -75 years, 12 females) diagnosed with isolated or combined movement disorders including dystonia and associated HMDs (i.e. tremor, myoclonus, chorea, tics, athetosis, stereotypies, ballismus) reflecting the targeted population to be assessed by the CODY-SAMP composite scale and four healthy controls were enrolled in the study. The demographics and clinical characteristics are detailed in **Table 1**. Video recordings were prospectively collected from routine clinical visits at the movement disorders clinic of the Service of Neurology, Montpellier Beau Soleil Clinic, France. Regulatory approvals were granted for the study (CESS-RESS 22075132 Bis and CNIL 2238428). All the participants underwent video recording sessions aimed to be performed under standardized condition, camera positioning, and consistent distance between participants and the camera to minimize variability. However, the total duration of video recordings varied among patients due to the impact of the movement disorders severity on task execution and completion time. Videos were captured using smartphone cameras capable of maintaining consistent frame rates (minimum of 30 frames per second, FPS) and resolution (1920×1080 pixels), ensuring adequate clarity for capturing subtle movements. Participants performed predefined, standardized motor tasks known to elicit or exacerbate motor phenomenology, including but not limited to resting, posture-holding tasks, and voluntary movements such as finger tapping, arm flexion/extension, target reaching, and writing. The complete content of the conditions and tasks captured in the video recordings is provided as supplementary material alongside the clinical scale. This acquisition setup was intentionally designed to reflect real-world clinic conditions (smartphone, routine exam), facilitating future telemedicine translation.

2.2 The composite clinical scale, CODY-SAMP

We developed a comprehensive composite clinical scale designed to systematically characterize the key features of motor phenomenology in patients with combined movement disorders, including dystonia. The scale is accompanied by a standardized video protocol (minimum duration: 12.5-minute) for clinical examination recording. The CODY-SAMP comprises three parts: (i) dystonia; (ii) associated HMD (tremor, myoclonus, chorea, tics, athetosis, ballismus, stereotypies); and (iii) hypokinetic movement disorders and other associated motor features (hypotonia, ataxia, pyramidal signs, dysarthria). For each core HMD, severity and frequency are quantified and associated neurological motor features are systematically documented. Detailed clinical assessment outcomes are not within the scope of the current work and are reported elsewhere. The HMDs indexed by Sections I and II of the CODY-SAMP constitute the movement disorder patterns targeted for recognition and classification by the DL models developed in this study.

2.3 Clinical Assessment and Annotation Protocol

Patients were clinically assessed by two physicians with expertise in movement disorders blinded to each other's assessments using the CODY-SAMP. They independently assessed the presence or absence of eight hyperkinetic involuntary movement disorders (HMDs): dystonia, tremor, myoclonus, chorea, athetosis, tics, ballismus, and stereotypies. Following the independent ratings, both clinicians met to review any discrepancies and establish a final consensus label (presence vs. absence) for each HMD, which served as the ground truth for subsequent analyses. Ten-second temporal windows defined based on clinician annotations specifying start and end times were automatically extracted from the complete video recordings of all twenty-one enrolled subjects. Fixed 10-second windows duration has been selected as a practical compromise since long enough to provide stable statistical, spectral, and complexity features for classification, while still short enough to capture the temporal fluctuations typical of HMDs. Further the administration of the clinical scale, clinicians annotated video segments using a predefined rule, marking clear presence ('1'), absence ('0'), or uncertainty ('2') for each HMD. Only segments marked explicitly as present or absent were included in the subsequent analysis; segments containing uncertain annotations were discarded to maintain data integrity. This rule ensured clear ground-truth labels for training and evaluation, however, reduces the annotation variability typically encountered in clinical practice. Data cleaning procedures were applied to remove any segments containing missing or non-numeric values. **Table 1** summarizes the video data characteristics for all patients, including the number of annotated 10-second windows, total video duration, and the total number of frames analyzed for each patient. Each HMD pattern was evaluated across three distinct conditions: at rest, during posture maintenance, and during with actions. Healthy control subjects underwent clinical examinations to exclude any movement disorder or other neurological or extra-neurological findings that would preclude their inclusion in the control group.

2.4 Video Processing and Feature Extraction Pipeline

Each video recording was processed individually, frame by frame, using OpenCV (cv2) to ensure consistent and reproducible extraction of spatiotemporal features (**Figure 1**). For each video, frame-level metadata were systematically extracted, including frame rate (frames per second; FPS), spatial resolution (width and height in pixels), and temporal indices (timestamp) for each frame. Timestamps were operationally defined as the cumulative elapsed time (in seconds) from video onset, initialized at $t=0$ for the first frame and incrementing by approximately 0.033 seconds per frame. This temporal resolution corresponds to a sampling rate of approximately 30 Hz (30 frames

Table 1. Summary of Patient Demographics, Diagnoses, and Video Data Characteristics. Etiology was confirmed in 33% of cases, an expected finding consistent with rates of etiologic diagnostic confirmation reported in the literature.

Patient	Age (y)	Gender	Diagnosis	Motor phenomenology	Number of 10-second windows (from annotations)	Total video duration	Number of frames
1	51	M	Combined dystonia	Cervical dystonia and action tremor	97	16min 32s	29787
2	55	M	Combined dystonia	Generalized dystonia, ataxia, myoclonus	103	17min 27s	31469
3	27	F	Hypoxic cerebral palsy	Generalized dystonia, spasticity, atetosis	131	22min 08s	39636
4	36	M	DIP2B gene related mixed movement disorder	Generalized dystonia, chorea, ataxia and atetosis	150	25min 25s	46005
5	34	M	DIP2B gene related mixed movement disorder	Generalized dystonia, chorea, with ataxia	121	20min 19s	36617
6	69	F	Combined dystonia	Progressive cranial dystonia, mild ataxia, action tremor	107	18min 09s	32695
7	25	M	Hyperkinetic movement disorders	Myoclonus, tics, tremor	109	18min 31s	33355
8	60	F	LRRK2 gene related Parkinson's disease	Parkinsonism and dystonia	97	16min 16s	29323
9	73	F	Dystonia	Generalized dystonia, mild ataxia	114	19min 02s	34288
10	71	F	Chorea-dystonia	Generalized chorea, focal dystonia	127	21min 20s	35396
11	20	F	ADCY5 gene related mixed movement disorder	Generalized dystonia, chorea, myoclonus	95	15min 51s	28556
12	75	F	Cerebellar and ataxia	Generalized dystonia, ataxia	115	19min 16s	34172
13	62	F	Dystonia	Generalized dystonia	104	17min 24s	34327
14	22	M	Tremor prominent movement disorder	Action tremor, dystonia	108	18min 01s	32456
15	63	F	Chorea-dystonia	Dystonia, chorea	115	19min 18s	34736
16	69	F	Combined dystonia	Generalized dystonia, mild parkinsonism	105	17min 36s	31699
17	70	F	Dystonia	Generalized dystonia	114	19min 07s	34433
18	37	M	TPPA gene related ataxia with vitamin E deficiency (AVED)	Ataxia, cervical dystonia	119	19min 58s	35965
19	26	M	Neurodevelopmental disorder and tardive dystonia	Dystonia, akathisia	105	17 min 22 s	31275
20	17	F	Myoclonus dystonia	Dystonia, myoclonus	99	16 min 27 s	29618
21	23	M	TIMMS gene related combined movement disorder	Generalized dystonia, tremor, spasticity, tics	102	16 min 54 s	30428

per second). Although minor temporal variability may occur due to codec compression or file export artifacts, the resulting time series reliably preserves the temporal structure of the source video data and enables precise temporal alignment of extracted features with clinical annotations. This approach facilitates precise, frame-level temporal analysis throughout the subsequent computational stages of the processing pipeline. Feature extraction was implemented in Python (version 3.10.17), leveraging established computational libraries^{17,31–38} to ensure analytical accuracy, methodological reproducibility, and computational efficiency. **Table 2** provides the major computational methods and tools employed across the end-to-end pipelines for video-based HMD classification^{17–21,24,31,32,34–42,43}. For each processing stage, ranging from video loading and frame-by-frame extraction, pose estimation, and feature engineering to supervised classification and evaluation, the table details the primary open-source software libraries used, relevant literature references, intended goals, expected effects, and known limitations or sources of error.

Table 2. Overview of Computational Methods, Libraries, and Challenges Identified in the Video-Based HMD Classification Pipeline.

Method	Library	In Reference	Goal	Effect	Problem
Video loading / extraction	OpenCV (cv2)	Bradski, 2000 / Cao et al., 2019	Load video files, extract metadata and frames	Enables frame-by-frame reproducible processing	Varying codecs, dropped frames
Frame-by-frame processing	OpenCV (cv2)	Bradski, 2000 / Cao et al., 2021	Sequential access to each frame, maintain temporal order	Ensures precise temporal correspondence	Frame drops, timing jitter
2D pose estimation	YOLOv8 (Ultralytics)	Redmon et al., 2016 / Jocher et al., 2023 / Mathis et al., 2018	Detect human keypoints in each frame (pose estimation)	Fast, accurate localization of body landmarks	Occlusion, rare postures, lighting
Numerical feature extraction	NumPy, SciPy	Harris et al., 2020 / Virtanen et al., 2020	Compute time series features: mean, standard deviation, differences, etc.	Enables quantitative description of motor behavior	Tracking noise, artifacts
Data augmentation	imageio	McKinney, 2010	Organize data samples in structured tables	Facilitates reproducibility	Memory usage for large datasets
Statistical feature engineering	pandas, NumPy, SciPy	Bandt & Pompe, 2002 / Harris et al., 2020 / Virtanen et al., 2020	Summarize displacement signals: mean, std, median, etc.	Captures variability, trends, central tendency	Sensitive to outliers
Specified feature extraction	SciPy (FFT)	Harris et al., 2020 / Zhang et al., 2022 / Bandt & Pompe, 2002	Detect rhythmicity, FFT dominant frequency, peak amplitude	Identifies tremor, periodic/oscillatory patterns	Noise, spectral leakage
Non-linear component features	libt, entropy (Python packages)	Bandt & Pompe, 2002	Assess nonlinearity: fractal dimension, permutation entropy	Quantifies complexity	Computational overhead, parameter selection
Data merging / label integration	pandas	McKinney, 2010	Merge clinical labels and extracted features	Enables supervised learning, outcome assignment	Label errors, systematization issues
Inbalance handling	imblearn (SMOTE), sklearm	Chawla et al., 2002	Address class imbalance (undersampling, SMOTE)	Improves minority class detection	Risk of overfitting, synthetic artifacts
Preprocessing (scaling, imputation)	scikit-learn	Pedregosa et al., 2011 / Vasquez, 2024	Normalize, standardize features, impute missing values	Consistent feature scaling, reduces bias	Selecting features affects outcome
Hyperspace dimension reduction (Grid Search)	scikit-learn	Breiman, 2001 / Pedregosa et al., 2011 / Chen & Guestrin, 2016 / Breiman, 2001 / Vasquez, 2024	Systematic search for the best hyperparameters	Maximizes model performance, reproducibility	Objective, reproducible symptom classification
Downstream analysis/classification	scikit-learn, XGBoost, LightGBM	Pedregosa et al., 2011 / Chen & Guestrin, 2016 / Breiman, 2001 / Vasquez, 2024	ML on extracted features: SVM, RF, MLP, KNN, XGB, LGBM, LR	Stratified (grouped/multilabel) for robust validation	Model generalization, overfitting
Cross-validation	scikit-learn, iterstrat	Niculescu-Mizil & Caruana, 2005	Assess data leakage, ensures patient independence	Prevents data leakage, ensures patient independence	Small fold size, variance
Performance metrics/evaluation	scikit-learn, numpy	Niculescu-Mizil & Caruana, 2005	Assess classifiers: F1, ROC-AUC, accuracy, bootstrapped CI	Quantifies model performance, reliability	Metric choice, statistical power

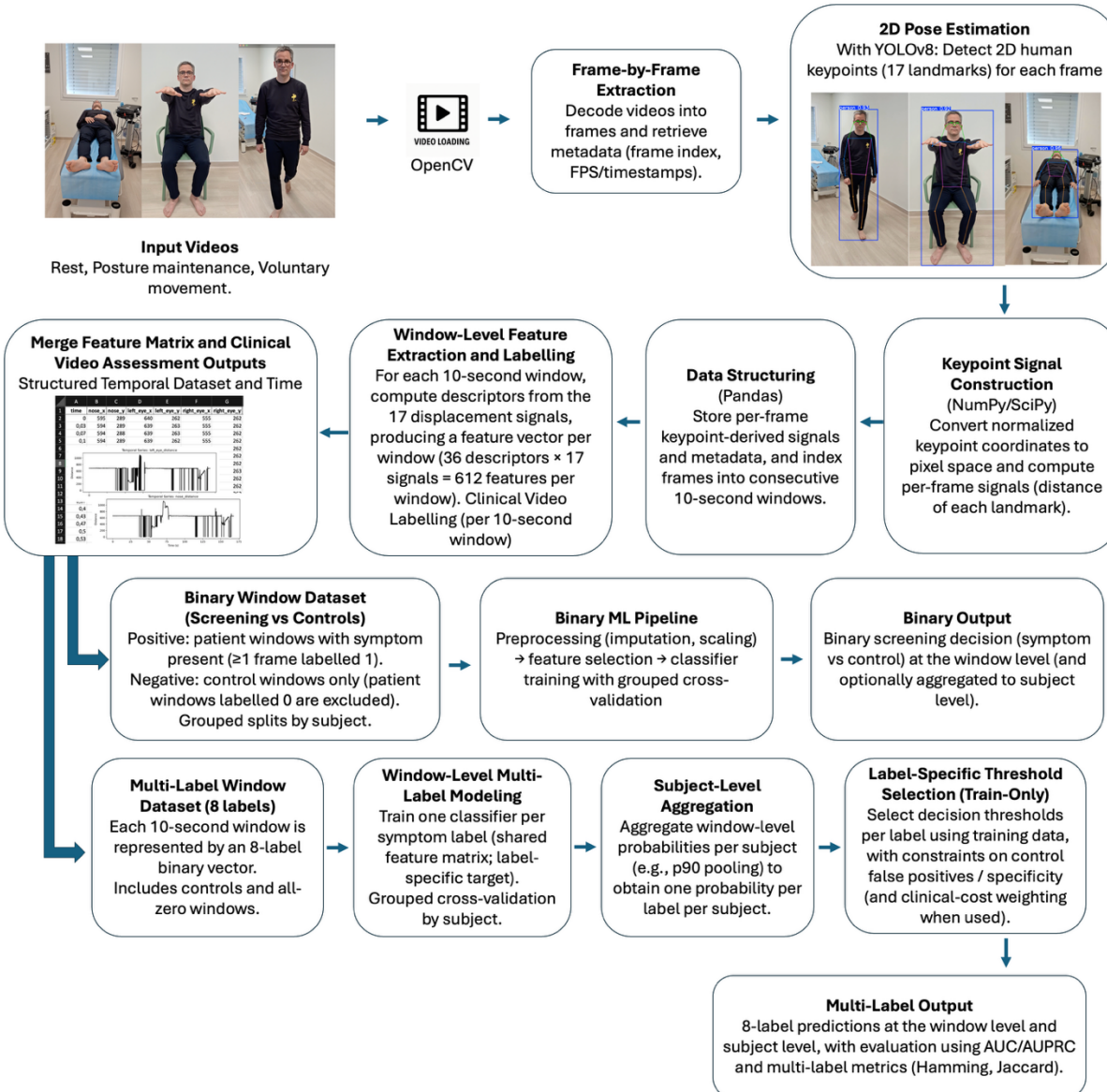


Figure 1. Schematic overview of the video-to-classification pipeline for automated detection of hyperkinetic movement disorders (HMDs). Clinical videos are decoded frame-by-frame using OpenCV, and 2D human pose estimation is performed with YOLOv8 to detect 17 anatomical keypoints per frame. Keypoint coordinates are converted to pixel space and used to construct per-frame signals, including landmark displacement signals. Frames are indexed into consecutive 10-second windows and stored using pandas. For each window, statistical, temporal, spectral and complexity descriptors are computed from each displacement signal, yielding a window-level feature vector. Clinical expert annotations are aligned with the extracted features at the 10-second window level, with uncertain segments excluded. From this merged window-level dataset, two analysis branches are derived: (i) a binary screening dataset contrasting symptom-positive patient windows against control windows, and (ii) an 8-label multi-label dataset where each window is represented by a symptom-prediction vector (including controls and all-zero windows when enabled). In the multi-label branch, one model is trained per symptom label at the window level; window-level probabilities are then aggregated at the subject level (e.g., p90 pooling) and label-specific decision thresholds are selected using training data under constraints on control false positives/specificity. Performance is evaluated using ROC-AUC/AUPRC and multi-label metrics (e.g., Hamming and Jaccard). Example images and schematic outputs are shown using data from a healthy control who provided informed consent for publication.

2.5 Key-point based models and Human Pose Estimation with YOLOv8

To quantify HMDs phenomenology from routine clinic videos, we relied on a keypoint-based representation of human pose, which is conceptually close to what clinicians observe at the bedside: the trajectories of recognizable anatomical landmarks over time (e.g., wrists, elbows, shoulders, hips, knees, ankles, and cranial points). Pose estimation was performed using YOLOv8 (*yolov8x-pose-p6.pt*), a state-of-the-art deep learning architecture for 2D keypoint detection in unconstrained settings (**Figure 1**). The model is pre-trained on large public datasets (e.g., COCO keypoints), enabling the detection of 17 standardized anatomical landmarks across distinct body parts: cranial, upper limb, trunk, and lower limbs. For each video frame, YOLOv8 outputs normalized 2D coordinates $(x, y) \in [0, 1]$ for each landmark, reflecting its position within the image. These were converted to absolute pixel coordinates by scaling with the original frame width and height, preserving spatial precision at the image level. Keypoints were stored in a structured dataset (pandas DataFrame; one row per frame), together with metadata required for temporal alignment and downstream analyses (frame timestamp, frame index, and video identifier). We exported these pose time series to spreadsheet format (.xlsx). The resulting datasets, raw landmarks, derived displacement signals, and metadata (**Table 3**), served as input for feature computation, normalization, and machine learning-based symptom classification. This representation explicitly bridges bedside phenomenology and computation: instead of learning from raw pixels, the model learns from the time-varying trajectories of clinically meaningful body points (e.g., distal vs proximal segments), facilitating anatomical interpretability (e.g., upper-limb predominant rhythmic oscillations vs irregular multi-segmental movements).

Table 3. Overview of Extracted Features from Video Pose Estimation and Time Series Analysis. This table summarizes the different types of features extracted from the pose estimation and time series processing pipeline applied to each video recording. For each feature type, the table reports the number of features computed, their specific names or examples, and a brief description of their methodological role in the dataset. This multi-level feature extraction approach enables a comprehensive and physiologically meaningful characterization of movement dynamics for subsequent machine learning analysis.

Feature type	#	Example / names	Methodological role	Clinical interpretation (bedside meaning)
Anatomical landmarks (2D keypoints)	17	None, eyes, ears, L/R shoulder, elbow, wrist, hip, knee, ankle	Frame-wise detection of anatomical body landmarks	Topography: where movement occurs (distal vs proximal, cranial vs appendicular involvement)
Landmark displacement signals (image-plane)	12	$d_{i,t} = \sqrt{(x_i - x_{i,t})^2 + (y_i - y_{i,t})^2}$ (mean, median, standard deviation, range, R ² , variance, skewness, kurtosis, energy, zero-crossings)	Converts 2D trajectories into relevant scalar time series signals	Topography/instability proxy: how much each body part moves over time
Statistical descriptors	12		Temporal distribution and variability of each displacement signal	Alterations/interruptions: jerk or burst-like events (myoclonus, fits), progressive change during tasks (task exacerbation/fatigability)
Temporal / dynamic features	3 (+ rolling means)	slope, mean absolute acceleration, rolling means ($w = 3, 5, 7$)	Capture trends, abrupt changes, and short-term variability	Topography/instability proxy: how much each body part moves over time
Spectral features	2	Fourier power spectrum	Quantify periodicity	Irregular/chaotic motion: higher complexity often aligns with non-rhythmic hyperkinetics (e.g., choreo-like components) vs more stereotyped patterns
Non-linear / complexity features	2	Hausdorff fractal dimension, permutation entropy	Quantify irregularity/complexity beyond simple variance	Context of observation: rest vs posture vs action for clinically meaningful stratification
Metadata	4	Timestamp, frame index, video ID, condition (Rest/Posture/Action)	Temporal alignment and stratified analyses	

2.6 Derived Additional Time-Series Features from landmark trajectories

Beyond raw keypoint coordinates, we derived clinically motivated time-series descriptors from each landmark trajectory to capture movement properties routinely assessed at the bedside, namely the magnitude and variability of movement, the presence of oscillatory pattern, and the degree of irregularity or complexity. For each anatomical landmark tracked in 2D with pixel coordinates (x_t, y_t) at frame t , we constructed a scalar displacement signal $d_t = \sqrt{x_t^2 + y_t^2}$. This representation provides a proxy of visible motion in standard clinical videos: while it does not correspond to 3D biomechanical displacement, it quantifies how much a segment moves in the camera plane under realistic acquisition conditions and, critically, retains segmental topography (cranial versus appendicular, proximal versus distal) that is central to clinical phenotyping of hyperkinetic movement disorders.

Trajectories were segmented into fixed-length windows aligned to expert labels, and within each window we computed a panel of descriptors designed to summarize clinically meaningful aspects of movement. First, to capture amplitude and instability, we extracted distributional summaries of $\{d_t\}$ including central tendency (mean and median), dispersion (standard deviation, variance,

interquartile range, and range), and extremes (minimum and maximum). We additionally computed skewness and kurtosis to reflect distributional asymmetry and tail behaviour, as well as signal energy $E = \sum_t d_t^2$, which acts as an integrated measure of movement burden over the observation window. These statistics correspond closely to clinical impressions of sustained displacement, variability around a postural set-point, and the presence of episodic high-amplitude displacements. Second, to capture temporal dynamics relevant to initiation, persistence and abruptness, we quantified linear drift through the slope of a least-squares regression of d_t over time, providing a simple measure of gradual postural change versus stability. We also computed mean absolute acceleration using second-order finite differences, which is sensitive to sudden changes in movement magnitude and therefore highlights paroxysmal events such as jerks. To better distinguish sustained deviations from transient spikes, we computed rolling means with short windows ($w \in \{3, 5, 7\}$), which capture persistent bias robust to momentary artefacts. Finally, we measured direction-change propensity by counting sign changes in first differences $\Delta d_t = d_{t+1} - d_t$, reflecting repeated reversals along the displacement trajectory, a property that can be clinically salient for differentiating slowly evolving writhing trajectories from more monotonic drifts. Third, to capture rhythmicity, we applied the Fast Fourier Transform (FFT) to each windowed displacement signal and extracted the dominant frequency and corresponding peak amplitude. Dominant frequency was defined as the frequency of the largest spectral peak excluding the 0-Hz (DC) component, which primarily reflects the mean signal level rather than rhythmic oscillations. These features provide a direct, interpretable quantification of oscillatory structure classically associated with tremor and certain patterned motor behaviours, while acknowledging that frequency estimates in short windows can vary with recording conditions and task context. Fourth, to quantify irregularity and complexity beyond simple dispersion or periodicity, we computed Higuchi fractal dimension and permutation entropy, which characterize scale-invariant irregularity and temporal disorder, respectively. In clinical terms, these measures capture the extent to which a trajectory appears stereotyped and predictable versus complex, irregular or chaotic, which is often invoked when describing chorea or mixed hyperkinetic states. For each window and each landmark displacement signal, this implementation computes 19 primary descriptors (distributional + temporal + spectral + entropy + complexity) and 3 rolling-mean descriptors, yielding 22 features per landmark per window. With $J = 17$ landmarks, this corresponds to $22 \times 17 = 374$ derived features per window in the multi-label pipeline. Feature names followed a transparent convention *[side]_[landmark]_distance_[metric]* (for example, *right_shoulder_distance_max* or *left_knee_distance_perm_entropy*), facilitating direct clinical interpretation and mapping to anatomical regions.

To ensure interpretability at a level consistent with clinical reasoning, we organized derived features into clinically grounded kinematic families and coarse anatomical regions. Kinematic families were defined to reflect the typical components of bedside movement description: baseline posture (central tendency metrics capturing the postural set-point), sustained bias (rolling-mean descriptors capturing persistent deviation robust to transient spikes), excursions (minimum and maximum values reflecting brief, high-amplitude displacements), variability (dispersion metrics summarizing movement magnitude and instability), rhythmicity (dominant FFT frequency and amplitude capturing oscillatory structure), directionality (trend and reversal proxies reflecting evolving trajectories and repeated changes in direction), and irregularity/complexity (non-linear and higher-order descriptors including permutation entropy and fractal dimension, as well as descriptors sensitive to abruptness and distributional shape). Anatomical regions were defined from the landmark identity and grouped into cranial, upper limb and lower limb, providing a clinically intuitive summary of where discriminative movement evidence was expressed in the field of view. Detailed mapping rules and the full feature list are provided in the Supplementary Material (**Supplementary Methods**). We quantified feature importance at the patient level using a decision-centric permutation approach

computed exclusively on the held-out outer test folds, thereby preventing information leakage. For each outer fold, baseline predictions were generated through the full inference pathway used in the primary analysis: window-level probabilities were computed by the fitted model, aggregated to patient-level probabilities using p90 pooling, and converted into binary patient-level decisions using label-specific clinical thresholds. Feature importance was then assessed by permuting one feature at a time in the held-out test data, re-running the same inference pathway without retraining, and measuring the increase in patient-level decision error, defined as $\Delta\text{error} = \text{error}_{\text{permuted}} - \text{error}_{\text{baseline}}$ with $\text{error} = (FP + FN)/N_{\text{patients}}$. This definition aligns attribution with the clinical decision boundary; as a consequence, many perturbations do not flip any patient decision and therefore yield near-zero Δerror , which reflects the discrete nature of thresholded clinical decision-making rather than an absence of predictive signal. For visualization and robustness, we summarized importances across folds by reporting mean Δerror and retained positive contributions, corresponding to perturbations that worsened decisions. We further applied a stability criterion requiring consistent contributions across outer folds before aggregating importance within kinematic families and anatomical regions. Group-level contributions were normalized within each symptom to report the share of total positive Δerror attributable to each family or region, producing an interpretable, clinically oriented decomposition of decision evidence rather than a model-internal attribution that may not map to actionable clinical concepts.

2.7 Machine Learning-Based HMD Classification

2.7.1 Window-Based Binary Classification of Individual HMD Presence Versus Absence

To benchmark symptom detection from pose-derived features, we conducted a systematic evaluation of preprocessing and supervised learning strategies (**Supplementary Methods**) across the eight hyperkinetic movement disorder (HMDs) phenomenologies (**Table 2**). For each symptom, we formulated a binary window-level classification problem in which a 10-second window was labeled HMD-present if at least one frame within the window was annotated as symptom-positive (label = 1). Windows containing uncertain annotations (label = 2) were excluded. To construct a conservative negative class in this screening-oriented setting, windows labeled HMD-absent (label = 0) were retained only for healthy controls, whereas windows labeled 0 from patients were not included. This design therefore evaluates symptom-expressing patient windows against control windows, under routine acquisition conditions.

We compared four feature scaling approaches (StandardScaler, MinMaxScaler, RobustScaler, and PowerTransformer) to account for heterogeneous feature distributions. We evaluated a panel of supervised classifiers commonly used for structured biomedical data: gradient-boosted decision trees (XGBoost, LightGBM), Random Forest, linear models (Logistic Regression, SVM with RBF kernel), instance-based learning (K-Nearest Neighbors), and a multilayer perceptron (MLP). Hyperparameters were optimized by exhaustive grid search over predefined parameter grids.

To prevent subject-level information leakage, we used 5-fold StratifiedGroupKFold cross-validation (`shuffle = True, random state = 42`), ensuring that all windows from a given subject (patient or control) were assigned exclusively to either the training or test split within each fold. Class imbalance was handled within each training fold: when the relative difference between class sizes exceeded 20%, we applied random undersampling of the majority class to match the minority class size. For classifiers producing potentially uncalibrated probability estimates, probability calibration was applied using Platt scaling (sigmoid calibration) via a calibrated classifier wrapper with internal cross-validation on the training data.

Performance was quantified at the window level using accuracy, class-specific F1-scores (reported separately for the positive and negative classes), and ROC-AUC. In addition, we derived a subject-level decision by aggregating out-of-fold window predictions within each subject using a majority-vote rule ($\geq 50\%$ positive windows). We report subject-level correct classification rate, sensitivity, and specificity based on this aggregated decision. This aggregation reduces the influence of sporadic window-level errors when multiple windows are available per subject and provides a complementary subject-level summary alongside window-level performance. Because the negative class is derived exclusively from controls, results should be interpreted within this screening-versus-control framework rather than as symptom absence detection within patients.

2.7.2 Patient-Level Binary Classification Using Symptom-Enriched Aggregated Time Series

To complement window-level analyses with a subject-level summary, we implemented a patient-based binary classification framework in which each subject was represented by a single feature vector per symptom. For each recording and target symptom, we constructed a symptom-enriched time series by selecting and concatenating windows according to rater annotations. Windows containing uncertain labels (value = 2) for the symptom were excluded. For controls, all available windows were retained. For patients, only windows in which the symptom was annotated as present (i.e., at least one frame with label = 1 within the window) were retained. The retained windows were concatenated to form a single per-subject time series per anatomical landmark, thereby focusing the representation on segments that are clinically informative for the symptom under consideration. Subjects without any retained windows for a given symptom were excluded from the corresponding symptom-specific analysis.

From this concatenated signal, we extracted pose-derived time-series features spanning the same feature families as the window-based pipeline (statistical, temporal/kinematic, spectral, and complexity descriptors computed from landmark displacement signals), yielding one aggregated feature vector per subject and symptom. Subjects were assigned a binary label reflecting group membership in this patient-versus-control setting (controls = 0; patients = 1), and models were trained to discriminate symptom-expressing patient recordings from healthy controls.

To prevent information leakage, model evaluation used 5-fold StratifiedGroupKFold cross-validation (shuffle = True, random state = 42), ensuring that each subject contributed to either training or testing folds only. Feature scaling was applied within each training fold using one of four transformations (StandardScaler, MinMaxScaler, RobustScaler, PowerTransformer). The same panel of supervised classifiers (logistic regression, SVM, k-nearest neighbors, multilayer perceptron, random forest, XGBoost, LightGBM) was evaluated with exhaustive grid search over predefined hyperparameter grids. For classifiers with potentially uncalibrated probability estimates (notably SVM and random forest), probability calibration was performed using Platt scaling (sigmoid calibration) via a calibrated classifier wrapper with internal cross-validation on the training data. Performance was reported at the subject level using accuracy, class-specific F1-scores, and ROC-AUC. Because patient feature vectors were derived from symptom-positive windows, this patient-level analysis characterizes a “symptom signature” at the subject level rather than evaluating symptom absence within patients; it therefore complements, rather than replaces, the window-level analysis.

2.7.3 Condition-Specific HMD Detection

To reflect clinical examination practice, we stratified recordings into three predefined conditions commonly used during examination: (i) rest, (ii) posture maintenance, and (iii) voluntary move-

ment (e.g., finger-to-nose maneuver). For each condition and symptom, we constructed one condition-specific sample per subject by aggregating the corresponding annotated segments into a single merged time series and extracting the same pose-derived feature set. A subject-condition sample was labeled symptom-positive if the symptom was annotated as present (label = 1) in any frame within the merged series; samples containing uncertain labels (label = 2) were excluded. Classifier performance was evaluated using subject-grouped cross-validation within each condition, enabling direct comparison of detection performance across motor tasks. For probability calibration, sigmoid (Platt) calibration was applied when class counts within the training fold were sufficient to support internal calibration cross-validation.

2.8 Multi-label detection of concurrent HMDs

To emulate routine clinical assessment, we evaluated simultaneous detection of multiple HMD phenotypes from 10-s video windows using an eight-label output space (dystonia, tremor, myoclonus, chorea, athetosis, ballismus, stereotypies and tics). Each window was assigned an 8-dimensional binary label vector derived from expert annotations (label = 1 if the symptom was present at any time within the window; else 0). In this multi-label setting, we explicitly controlled false alarms in asymptomatic recordings by including control subjects and symptom-absent windows, enabling clinically interpretable subject-level readouts under a conservative operating regime.

Subject-level separation and multilabel-aware stratification. To prevent leakage and reflect deployment on unseen individuals, all evaluation splits were performed at the subject level: all windows from a given participant were assigned exclusively to either training or testing within each fold. Multi-label stratification was performed on subject-level label vectors obtained by a logical OR across windows per participant, thereby preserving both marginal label prevalence and common co-occurrence patterns across folds (MultilabelStratifiedKFold; shuffle with fixed random seed).

Model families and preprocessing. We benchmarked a panel of representative classifier families for structured biomedical data spanning linear, margin-based, instance-based and tree-ensemble methods, as well as multilayer perceptrons. Preprocessing consisted of feature scaling when appropriate (StandardScaler, MinMaxScaler, RobustScaler, PowerTransformer) followed by univariate feature selection using mutual information (SelectKBest; fixed K with minor label-specific adjustments; details in **Supplementary Methods**). When probability estimates were not natively available, probabilistic scores were obtained via Platt scaling to ensure a consistent probabilistic interface for downstream thresholding and aggregation. Class imbalance was handled using class-weighting when supported by the estimator.

From window probabilities to subject-level multi-label decisions. Each label was modelled as an independent binary task at the window level, yielding per-window probabilities for each symptom. To obtain a clinically actionable subject-level multi-label profile, window probabilities were aggregated within each subject using percentile pooling (90th percentile), producing one probability per subject and label. Decision thresholds were tuned per label on training subjects only using a clinically motivated operating-point policy that minimises a balanced error criterion under explicit constraints on false positives among control subjects (including label-specific constraints for high-impact phenotypes). Thresholds were then applied unchanged to held-out test subjects. In addition, we evaluated an optional nested selection strategy in which the best-performing model configuration could be selected independently for each label within the training data (inner cross-validation), reflecting the heterogeneous learnability and risk profile of the individual phenotypes.

Evaluation. Primary performance was reported at the subject level. Discrimination was quantified using macro-averaged ROC-AUC and macro-averaged average precision (AUPRC), computed

label-wise when both classes were present in the test fold and then averaged across eligible labels. For binary predictions, we reported micro- and macro-averaged F1-scores, sample-wise Jaccard index and Hamming accuracy for the full 8-label vector. Per-label precision, recall, specificity and F1-score were also reported, and control-only false positives were tracked to verify alignment with the targeted operating regime.

2.8.1 Focused HMD detection: dystonia versus athetosis versus chorea versus control

To further assess the pipeline in a clinically relevant scenario of overlapping HMD, we implemented a focused four-class classification task. Ten-second windows were annotated as dystonia, chorea, athetosis, or control (no symptom). Only windows with unambiguous labels were retained for analysis. The same optimized feature extraction and classification pipeline was applied, with patient-grouped cross-validation to prevent leakage across subjects. Performance metrics included the positive-class F1-score for each category and macro-averaged ROC-AUC, enabling direct assessment of discriminability between chorea, athetosis, and controls.

2.9 Implementation and Computation

The pipelines described in our study were implemented using Python (version 3.10.17). All related Python scripts and results are provided on GitHub: <https://github.com/xaviervasques/CODY>

3 Results

We developed and evaluated a pose-based machine-learning pipeline for automated detection and phenotyping of HMDs from routine clinical videos. The pipeline converts 2D pose keypoints into anatomically meaningful displacement time series and computes interpretable window-level kinematic descriptors, spanning statistical, temporal, spectral, and complexity features. Models from several classifier families were benchmarked and optimized using cross-validated hyperparameter search under patient-grouped splits to prevent leakage.

Results are organized into three complementary components. First, we performed window-level screening in a case-control design, contrasting symptom-positive patient windows against healthy control windows for each HMD phenotype, and report window- and, when applicable, subject-level decisions obtained by aggregating repeated windows per participant. Second, we predicted concurrent symptom profiles across eight labels at the window level and derived patient-level multi-label profiles by aggregating window probabilities using percentile pooling (p90), followed by label-wise thresholding tuned on training subjects under control-aware constraints to yield clinically meaningful operating points. Third, we analyzed the contribution and interpretability of the engineered kinematic descriptors (e.g., feature families and/or feature importance across models and phenotypes), providing insight into which motion signatures drive classification performance.

Across all experiments, model selection and evaluation relied on patient-level cross-validation splits, ensuring that no participant contributed data to both training and testing partitions. We report the best-performing preprocessing-classifier combinations using discrimination and error-sensitive metrics appropriate to each setting (e.g., ROC-AUC/AUPRC and F1 for binary detection, Hamming/Jaccard for multi-label prediction), alongside subject-level sensitivity/specificity where relevant.

3.1 Window-Level Detection of Individual Movement Disorders

Table 4 and **Figure 2A** summarize the best-performing window-based pipelines for each HMD using 10-s video segments. In this screening-oriented evaluation, symptom-expressing patient windows (at least one symptom-positive frame within the 10-s window) were contrasted against control windows, while windows containing uncertain annotations were excluded. The analysis quantifies how well pose-derived time-series features discriminate clinically labeled symptom expression from normative movement patterns in controls, rather than testing symptom absence within patients.

Across phenotypes and annotation sets, models showed consistently high subject-level specificity after within-subject aggregation (1.00 for all symptoms and raters), indicating that healthy controls were rarely labelled as symptomatic once window-level predictions were integrated at the subject level. This behaviour is clinically desirable in a screening context, where the cost of false alarms can be substantial; it also suggests that pose-derived features capture stable normative movement patterns that are not easily misclassified as hyperkinetic activity when evidence is pooled across repeated short segments.

Window-level discrimination nevertheless varied by phenotype, mirroring differences in movement phenomenology and the ease of defining symptom boundaries on video. Dystonia, chorea, tremor and tics exhibited robust window-level performance and reliable subject identification, consistent with relatively distinctive kinematic signatures, sustained abnormal posturing for dystonia, irregular purposeless excursions for chorea, rhythmic oscillatory structure for tremor, and brief stereotyped bursts for tics. In contrast, athetosis, stereotypies, myoclonus and ballismus were more challenging at the 10-s window scale, consistent with (i) slow, continuous and often mixed-pattern movements (athetosis), (ii) context-dependent and heterogeneous repetitive behaviours (stereotypy).

ies), and (iii) highly intermittent, short-duration events that can be difficult to time-stamp consistently (myoclonus and ballismus). Notably, ballismus showed the weakest window-level reliability, in line with its rarity and episodic expression in the cohort, which limits the number of informative positive windows and increases estimator variance.

Importantly, subject-level identification generally exceeded window-level reliability, supporting the clinical utility of aggregating repeated short observations. Majority-vote aggregation reduces the influence of sporadic window-level errors and recapitulates the clinical process of forming a judgement after reviewing multiple epochs rather than relying on a single short clip. This effect is most apparent for phenotypes with intermittent expression, where individual windows may be uninformative despite the overall examination containing sufficient evidence of symptom presence.

3.1.1 Symptom-Specific Performance Insights

Dystonia demonstrated strong and consistent performance across annotation sets ($F1_1 = 0.84$ vs 0.89 ; patient sensitivity = 0.92 vs 1.00), supporting the presence of stable pose-derived kinematic signatures that are reproducibly captured despite rater-specific labeling policies. Chorea was also robust ($F1_1 = 0.81$ vs 0.96) with perfect patient-level sensitivity in both annotation sets; the larger between-annotation performance difference at the window level ($\Delta F1 \approx 0.15$) is consistent with subtle differences in labeling thresholds for borderline choreiform movements. Tremor performance was highly concordant across annotation sets ($F1_1 \approx 0.82$ – 0.83 ; $\Delta F1 \approx 0.01$) with strong patient identification (≈ 0.89 – 0.92), in keeping with a relatively rhythmic motor signature. Tics achieved excellent patient-level detection in both annotation sets (patient sensitivity = 1.00), despite greater variability at the window level for Rater 1 ($F1_1 = 0.75 \pm 0.25$), likely reflecting limited numbers of positive windows and the intermittent nature of tic expression.

In contrast, athetosis yielded only moderate window-level performance ($F1_1 = 0.59$ vs 0.49) with reasonable patient sensitivity (0.80 vs 0.75), consistent with its continuous, flowing phenomenology and overlap with other hyperkinetic patterns. Ballismus was the most challenging phenotype ($F1_1 = 0.14$ vs 0.23), with marked annotation-set dependence in patient sensitivity (1.00 vs 0.50), compatible with rarity and episodic expression as well as ambiguity in defining ballistic segments. Stereotypies showed moderate performance in the single available annotation set ($F1_1 = 0.54 \pm 0.26$; patient sensitivity = 0.75), reflecting heterogeneous and context-dependent repetitive patterns. Finally, myoclonus was strongly annotation-set dependent ($F1_1 = 0.68$ vs 0.36 ; patient sensitivity = 0.90 vs 0.43 ; $\Delta F1 \approx 0.32$).

3.1.2 Patient-Level Classification Through Window Aggregation

The “percentage of subjects correctly classified” (**Table 4** and **Figure 2A**) quantifies subject-level discrimination between symptom-expressing patients and healthy controls obtained by aggregating out-of-fold window predictions within each subject. Each 10-s window is classified independently, and a subject is labelled “symptom-positive” when at least half of their windows are predicted positive ($\geq 50\%$). Clinically, this parallels a physician reviewing multiple short epochs before issuing an overall judgement based on the preponderance of evidence. Subject-level performance was consistently high across most phenotypes and annotation sets, frequently reaching 1.00 , indicating that aggregation mitigates sporadic window-level errors, particularly for intermittent phenotypes, while preserving conservative behavior in controls.

3.1.3 Performance Under Standardized Clinical Conditions

To assess robustness across standardized examination contexts, we evaluated symptom-versus-control classification separately during rest, posture maintenance, and action. As summarized in **Figure 2B**, dystonia and tremor remained highly discriminable across conditions for several model families, with multiple pipelines achieving near-ceiling performance. Given the smaller condition-specific subsets, these results should be interpreted as supportive evidence of context robustness.

Table 4. Window-based binary classification of HMD symptom expression in 10-second video windows (screening versus controls). This table summarizes the performance of window-based classifiers for each HMD phenotype under two independent clinician annotation sets. For each phenotype and rater, the best-performing scaler–classifier pipeline is reported. Evaluation used 5-fold StratifiedGroupKFold cross-validation with subject-level splitting to prevent leakage. Window-level metrics (F1_1 for the positive class, F1_0 for the negative class, accuracy, and ROC-AUC) are reported as mean \pm SD across folds. Subject-level metrics are derived by aggregating out-of-fold window predictions within each subject using majority voting ($\geq 50\%$ positive windows), and include the percentage of correctly classified subjects, sensitivity among symptom-expressing patients included in the symptom-specific dataset, and specificity among controls. The mean \pm SD number of windows in training and test partitions is also reported. In this screening-oriented design, the negative class comprises control windows only (symptom-absent patient windows were not included).

Symptom	Rater	Scaler	Classifier	F1_1	F1_0	Accuracy	ROC_AUC	Subject-level accuracy (%)	Patient sensitivity	Control specificity	Windows (train)	Windows (test)
Dystonia	Rater_1	RobustScaler	RandomForest	0.84 \pm 0.08	0.73 \pm 0.04	0.81 \pm 0.06	0.88 \pm 0.06	94 \pm 24%	0.92	1.00	1892 \pm 92	473 \pm 92
Dystonia	Rater_2	PowerTransformer	RandomForest	0.89 \pm 0.02	0.84 \pm 0.06	0.88 \pm 0.03	0.93 \pm 0.05	100 \pm 0%	1.00	1.00	1606 \pm 126	402 \pm 126
Chorea	Rater_1	MinMaxScaler	LightGBM	0.81 \pm 0.18	0.93 \pm 0.08	0.90 \pm 0.11	0.95 \pm 0.06	100 \pm 0%	1.00	1.00	803 \pm 109	201 \pm 109
Chorea	Rater_2	StandardScaler	XGBoost	0.96	0.94	0.95	0.99	100 \pm 0%	1.00	1.00	690 \pm 80	173 \pm 80
Tics	Rater_1	MinMaxScaler	RandomForest	0.75 \pm 0.25	0.99 \pm 0.01	0.97 \pm 0.03	0.96 \pm 0.04	100 \pm 0%	1.00	1.00	387 \pm 48	97 \pm 48
Tics	Rater_2	StandardScaler	XGBoost	1.00	1.00	1.00	1.00	100 \pm 0%	1.00	1.00	394 \pm 78	98 \pm 78
Tremor	Rater_1	PowerTransformer	RandomForest	0.83 \pm 0.01	0.84 \pm 0.05	0.84 \pm 0.05	0.92 \pm 0.04	89 \pm 31%	0.83	1.00	817 \pm 92	204 \pm 92
Tremor	Rater_2	MinMaxScaler	RandomForest	0.82 \pm 0.02	0.87 \pm 0.01	0.85 \pm 0.01	0.92 \pm 0.02	92 \pm 27%	0.89	1.00	738 \pm 117	184 \pm 117
Athetosis	Rater_1	StandardScaler	XGBoost	0.59 \pm 0.30	0.92 \pm 0.02	0.87 \pm 0.05	0.94 \pm 0.02	89 \pm 31%	0.80	1.00	533 \pm 87	133 \pm 87
Athetosis	Rater_2	StandardScaler	MLP	0.49 \pm 0.14	0.86 \pm 0.05	0.79 \pm 0.05	0.78 \pm 0.09	82 \pm 39%	0.75	1.00	449 \pm 63	112 \pm 63
Ballismus	Rater_1	PowerTransformer	RandomForest	0.14	0.91	0.84	0.85	100 \pm 0%	1.00	1.00	562 \pm 77	141 \pm 77
Ballismus	Rater_2	StandardScaler	MLP	0.23 \pm 0.10	0.96 \pm 0.02	0.92 \pm 0.04	0.76	75 \pm 43%	0.50	1.00	556 \pm 49	139 \pm 49
Stereotypies	Rater_1	MinMaxScaler	LightGBM	0.54 \pm 0.26	0.96 \pm 0.02	0.92 \pm 0.04	0.84 \pm 0.15	88 \pm 33%	0.75	1.00	477 \pm 84	119 \pm 84
Myoclonus	Rater_1	MinMaxScaler	LightGBM	0.68 \pm 0.14	0.86 \pm 0.08	0.81 \pm 0.11	0.88 \pm 0.09	93 \pm 26%	0.90	1.00	534 \pm 121	134 \pm 121
Myoclonus	Rater_2	StandardScaler	KNN	0.36 \pm 0.02	0.89 \pm 0.05	0.81 \pm 0.07	0.72 \pm 0.07	64 \pm 48%	0.43	1.00	471 \pm 116	118 \pm 116

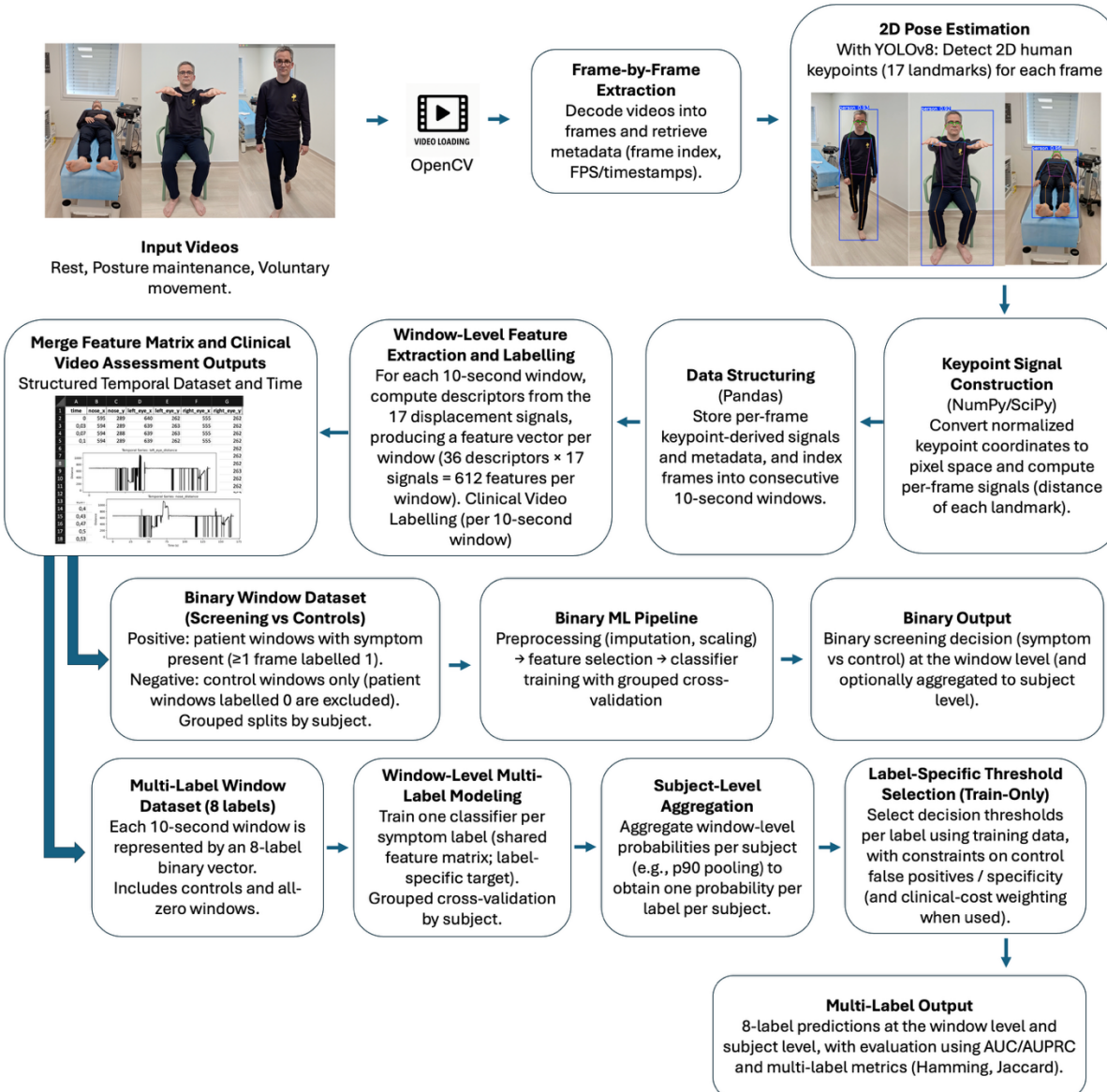


Figure 2. Window-based symptom classification performance and condition-specific comparison across rest, posture maintain, and with action. (A) Summary of the window-based binary classification of symptom presence versus absence for each hyperkinetic movement disorder. For each symptom, the table reports the mean F1-score for the positive class (averaged across available raters and shown with rater-specific values), the percentage of patients correctly identified at the patient level (derived from window-level predictions), and an inter-rater consistency indicator ($\Delta F1$ between raters; lower values indicate higher agreement). Cell background colors provide a qualitative performance cue (green = higher performance; orange = intermediate; red = lower; for $\Delta F1$, green = lower disagreement). (B) Performance of symptom classification pipelines evaluated on condition-specific 10-second segments, stratified by motor context (Rest, Action, Posture). For each symptom-condition pair, bars show the mean F1-score (positive class) \pm standard deviation across cross-validation folds for a single representative model per classifier family (XGBoost, LightGBM, RandomForest, Logistic Regression, SVM, k-NN, MLP), enabling direct comparison of model families and motor conditions.

3.2 Multi-label detection of concurrent hyperkinetic phenotypes

We next evaluated whether pose-derived kinematic features can support simultaneous, clinically interpretable detection of multiple hyperkinetic movement disorder (HMD) phenotypes, reflecting the reality that several abnormal movement patterns may co-occur within the same patient. All multi-label analyses were conducted on the consensus dataset, in which window-level annotations were harmonised across the two raters as described in the Methods, thereby reducing idiosyncratic rater effects and anchoring performance to a shared clinical ground truth. Predictions were generated at the 10-s window level and then consolidated into a subject-level multi-label profile via p90 pooling of window probabilities within each subject, followed by label-wise thresholding tuned exclusively on training subjects under a control-aware operating regime.

Across cross-validation folds, the best-performing pipeline selected by discrimination criteria achieved macro-AUPRC 0.821 ± 0.019 and macro-AUC 0.830 ± 0.029 at the patient level (**Table 6**; **Figure 3B**), indicating robust separability of symptomatic and asymptomatic individuals when probabilities are interpreted as ranked evidence rather than hard calls. Importantly, optimizing for different clinical priorities produced the expected trade-offs. The configuration yielding the highest Hamming accuracy (i.e., maximizing correctness of the full set of patient-label decisions) reached 0.764 ± 0.041 (**Table 6**; **Figure 3B**), whereas operating points designed to reduce clinical burden (lowest clinical cost) shifted performance toward conservative calling with broader uncertainty (**Table 6**). Taken together, these results indicate that the same probabilistic backbone can be tuned toward either “screening-like” sensitivity or “rule-in-like” specificity, depending on the intended clinical workflow.

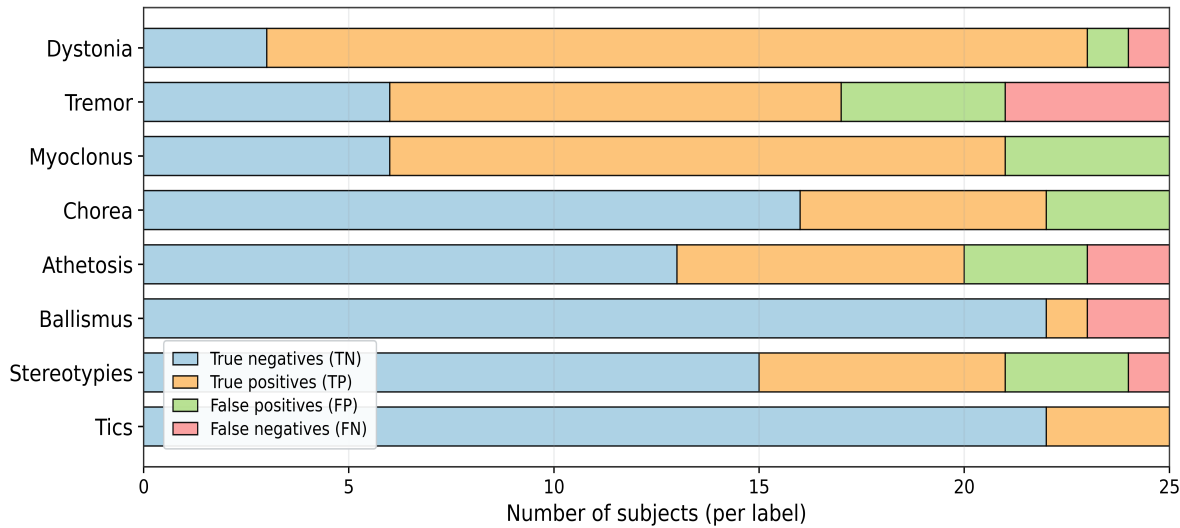
To contextualize these aggregate metrics, we examined the best per-label models (selected to minimize patient-level errors for each phenotype) and decomposed predictions into true negatives, true positives, false positives and false negatives (**Figure 3A**; **Table 5**). Considering that the evaluation comprises 200 patient-label decisions (25 subjects \times 8 labels), the per-label selection yields 28 total errors, corresponding to 172 correct decisions (86.0%) while preserving clinically interpretable error modes. Performance was strongest for phenotypes with distinctive and/or consistently annotated patterns: tics were perfectly identified in this cohort (TP=3, TN=22; no false positives or false negatives), and dystonia showed high sensitivity with only a single missed case (TP=20, FN=1) alongside minimal over-calling (FP=1) (**Table 5**; **Figure 3A**). Myoclonus and chorea also demonstrated high recall in this cohort (no false negatives), with remaining errors dominated by false positives, an error profile that, in practice, would be triaged by clinical context and could be mitigated by stricter operating points for phenotypes where false alarms are costly.

In contrast, the most clinically challenging phenotypes reflected familiar sources of ambiguity in routine assessment. Tremor exhibited the largest residual error burden (FN=4, FP=4), consistent with borderline presentations and overlap with dystonia and non-specific movement patterns captured in short windows; athetosis similarly showed balanced contributions of false negatives and false positives (FN=2, FP=3), suggesting that subtle, low-frequency fluctuations remain difficult to consolidate into an unambiguous patient-level call. For rare labels, the error decomposition was particularly informative. Ballismus, observed in only three positive subjects, maintained perfect specificity (FP=0) but lower sensitivity (FN=2), illustrating the expected behaviour of cautious detection in the low-prevalence regime: the model avoids over-calling a high-impact diagnosis at the expense of missed cases (**Table 5**; **Figure 3A**). This pattern reinforces the clinical value of reporting both sensitivity- and specificity-aligned summaries, rather than relying on a single scalar score.

Taken together, these results show that multi-label subject-level inference from pose-derived features is feasible under clinically motivated constraints, including the presence of control subjects

and symptom-absent windows, and that performance is best understood as a phenotype-specific operating landscape rather than a single scalar score. The consensus-label evaluation further indicates that the signal exploited by the models is not tied to one rater’s annotation, supporting the interpretation that the learned representations capture reproducible kinematic correlates of hyperkinetic phenomenology. The remaining errors, concentrated in a small set of ambiguous or rare phenotypes, provide a clinically actionable map of where additional data density, refined label definitions, or symptom-specific modelling is most likely to yield further gains.

A Best per-label models (patient-level, multi-label): decomposition into TN/TP/FP/FN



B Multilabel patient-level performance (p90 aggregation): best pipeline per comparator

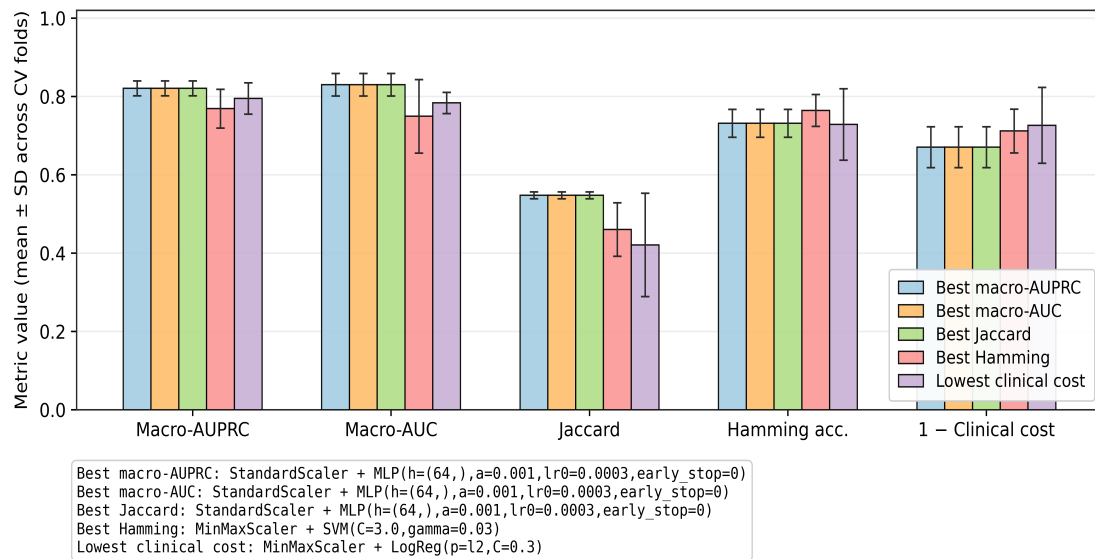


Figure 3. Patient-level multi-label performance for simultaneous detection of hyperkinetic movement disorders (HMDs) using p90 aggregation of window-level probabilities. (A) Confusion-matrix decomposition for the best-performing per-label pipelines, showing the number of subjects classified as true negatives (TN), true positives (TP), false positives (FP) and false negatives (FN) for each phenotype. Counts are reported at the subject level (total subjects per label = TN+TP+FP+FN) to highlight the relative contribution of correct detections and error types across phenotypes, with performance interpreted in the context of label prevalence. (B) Comparison of the best overall pipelines selected by different evaluation criteria (macro-AUPRC, macro-AUC, sample-wise Jaccard index, Hamming accuracy, and 1 - clinical cost), reporting mean \pm s.d. across cross-validation folds at the subject level. This panel illustrates that different operating objectives select different model configurations and summarizes the trade-offs between discrimination (AUC/AUPRC) and error-sensitive objectives (Jaccard/Hamming/clinical cost) under the same p90 subject-level aggregation and per-label thresholding policy.

Table 5. Best per-label patient-level classifiers and confusion-matrix decomposition (multi-label, p90 aggregation). For each hyperkinetic movement disorder phenotype (dystonia, tremor, myoclonus, chorea, athetosis, ballismus, stereotypies, tics), the table reports the single pipeline achieving the lowest patient-level error count for that label among all benchmarked models. We provide the number of positive (P) and negative (N) subjects and the corresponding prevalence, followed by the confusion-matrix components at the patient level (TP, FN, FP, TN). Error rates are summarized as false negative rate ($FNR = FN/(TP+FN)$) and false positive rate ($FPR = FP/(FP+TN)$), along with the total number of errors ($FP+FN$) and errors per patient ($\text{errors}/(P+N)$). Recall (sensitivity) and specificity are also reported to contextualize detection performance and false-alarm control.

Model	Label	P	N	Prevalence	TP	FN	FP	TN	FNR	FPR	Errors	Errors per patient	Recall	Specificity
MinMaxScaler + SVM(C=3.0,gamma=0.03)	Dystonia	21	4	0.84	20	1	1	3	0.047619048	0.25	2	0.08	0.952	0.75
StandardScaler + SVM(C=3.0,gamma=scale)	Tremor	15	10	0.6	11	4	4	6	0.2666666667	0.4	8	0.32	0.733	0.6
MinMaxScaler + KNN(k=9,w=uniform,p=2)	Myoclonus	15	10	0.6	15	0	4	6	0	0.4	4	0.16	1	0.6
MinMaxScaler + KNN(k=9,w=uniform,p=2)	Chorea	6	19	0.24	6	0	3	16	0	0.157894737	3	0.12	1	0.842
MinMaxScaler + KNN(k=9,w=uniform,p=2)	Athetosis	9	16	0.36	7	2	3	13	0.222222222	0.1875	5	0.2	0.778	0.813
StandardScaler + SVM(C=3.0,gamma=scale)	Ballismus	3	22	0.12	1	2	0	22	0.6666666667	0	2	0.08	0.333	1
StandardScaler + SVM(C=10.0,gamma=0.02)	Stereotypies	7	18	0.28	6	1	3	15	0.142857143	0.1666666667	4	0.16	0.857	0.833
MinMaxScaler + SVM(C=1.0,gamma=scale)	Tics	3	22	0.12	3	0	0	22	0	0	0	0	1	1

Table 6. Multi-label patient-level performance (p90 aggregation): best pipeline selected per comparator. This table summarizes patient-level multi-label performance for the top-performing pipeline under each model-selection criterion (“comparator”). Specifically, we identify (i) the pipeline maximizing macro-average AUPRC, (ii) the pipeline maximizing macro-average ROC-AUC, (iii) the pipeline maximizing the sample-wise Jaccard index, (iv) the pipeline maximizing Hamming accuracy, and (v) the pipeline minimizing the clinical cost. For each selected pipeline, results are reported as mean \pm standard deviation across cross-validation folds for macro-AUPRC, macro-AUC, Hamming accuracy, and micro- and macro-averaged F1-scores, providing a consolidated view of discrimination, multi-label agreement, and balanced classification performance under different operating-point priorities.

Best pipeline	Comparator	Macro-AUPRC	Macro-AUC	Hamming acc	Micro-F1	Macro-F1
StandardScaler + MLP(h=(64,),a=0.001,lr0=0.0003,early_stop=0)	Best macro-AUPRC	0.821 \pm 0.019	0.830 \pm 0.029	0.731 \pm 0.036	0.729 \pm 0.034	0.658 \pm 0.062
StandardScaler + MLP(h=(64,),a=0.001,lr0=0.0003,early_stop=0)	Best macro-AUC	0.821 \pm 0.019	0.830 \pm 0.029	0.731 \pm 0.036	0.729 \pm 0.034	0.658 \pm 0.062
StandardScaler + MLP(h=(64,),a=0.001,lr0=0.0003,early_stop=0)	Best Jaccard	0.821 \pm 0.019	0.830 \pm 0.029	0.731 \pm 0.036	0.729 \pm 0.034	0.658 \pm 0.062
MinMaxScaler + SVM(C=3.0,gamma=0.03)	Best Hamming	0.769 \pm 0.049	0.749 \pm 0.094	0.764 \pm 0.041	0.693 \pm 0.046	0.563 \pm 0.020
MinMaxScaler + LogReg(p=12,C=0.3)	Lowest clinical cost	0.795 \pm 0.040	0.784 \pm 0.027	0.729 \pm 0.091	0.656 \pm 0.118	0.632 \pm 0.158

3.2.1 Focused Multi-label Performance: Dystonia, Chorea, Athetosis and Controls

We trained and evaluated the multi-label approach restricted to dystonia, chorea, and athetosis, including healthy controls. To summarize the best attainable performance for each phenotype, we selected, within the evaluated model panel, the configuration that minimized patient-level errors (false positives + false negatives) for that specific label. For dystonia (prevalence 0.84; 21/25 patients), the best-performing model achieved 21/21 true positives with 0 false negatives and only 1 false positive among 4 negatives (errors/patient 1/25 = 0.04; FNR=0.00, FPR=0.25), with strong cross-validated discrimination (AUC=0.952, AUPRC=0.994) and F1=0.978. For chorea (prevalence 0.24; 6/25 patients), the best-performing model yielded TP=4, FN=2, FP=4, TN=15 (errors/patient 6/25 = 0.24; FNR=0.33, FPR=0.21), with AUC=0.790, AUPRC=0.583, and F1=0.567. For athetosis (prevalence 0.36; 9/25 patients), the best-performing model resulted in TP=7, FN=2, FP=3, TN=13 (errors/patient 5/25 = 0.20; FNR=0.22, FPR=0.19), with AUC=0.741, AUPRC=0.648, and F1=0.705. Collectively, these results indicate near-ceiling sensitivity for dystonia with minimal false alarms, whereas chorea and athetosis remain more challenging, consistent with lower prevalence and greater phenotypic overlap in routine outpatient videos.

When applying the same multi-model approach to the full symptom set, the error profile shifts in a phenotype-specific way. Chorea improves materially in the full panel (errors decrease from 6 \rightarrow 3), suggesting that additional phenotypes and richer negative structure can reduce ambiguity and help isolate chorea-specific kinematic signatures. Athetosis appears broadly stable, indicating that its separability is less sensitive to whether training is restricted or expanded. In contrast, dystonia performs slightly better in the reduced panel (difference of one additional error), which is consistent with dystonia being highly prevalent and heterogeneous: adding more phenotypes can introduce boundary competition, which may marginally increase confusion at the thresholded decision level

even when probability-level separability remains strong.

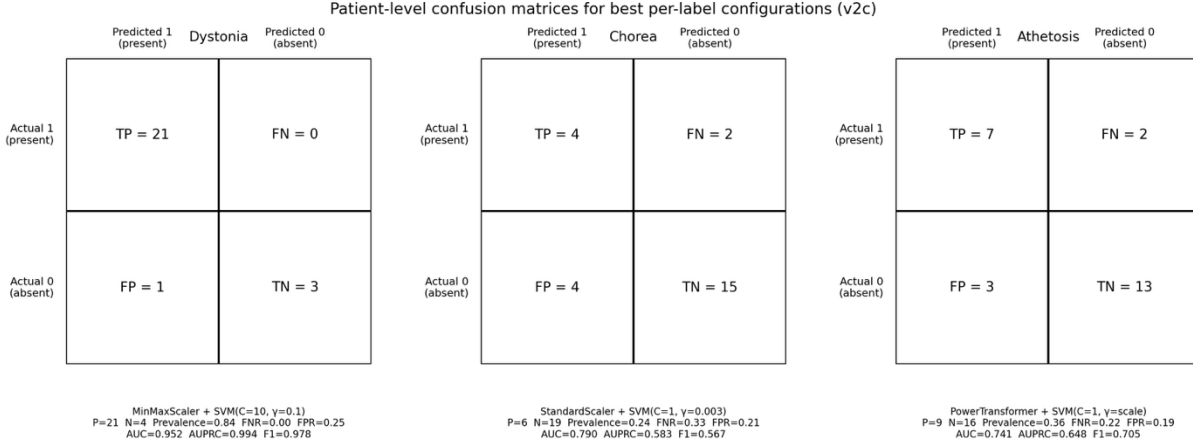


Figure 4. Patient-level performance for dystonia, chorea, and athetosis. For each phenotype, we report the confusion matrix (TP, FN, FP, TN) at the patient level, using the single best-performing model for that label as defined by the lowest patient-level error count (FP+FN). The top row corresponds to patients with the phenotype present in the ground truth (“Actual 1”), and the bottom row to phenotype absent (“Actual 0”); columns indicate model predictions (“Pred 1” vs “Pred 0”). In addition to error counts, each panel summarizes key discrimination and classification metrics computed from cross-validation (AUC, AUPRC, precision, recall, specificity, and F1). Dystonia shows near-perfect detection (no false negatives) with a single false positive, while chorea and athetosis exhibit higher residual error rates driven by both false positives and false negatives.

3.3 Clinically interpretable feature importance at the patient level

To identify which kinematic descriptors most strongly influenced clinically meaningful classification decisions, we quantified patient-level permutation importance on the held-out outer test folds only, thereby preventing information leakage. Importance was defined as the increase in patient-level decision error (Δ error, where $\text{error} = (\text{FP}+\text{FN})/N$ patients) induced by permuting one feature at a time while preserving the full inference pathway (window-level probabilities, p90 patient aggregation, and label-specific clinical thresholds). Because attribution was evaluated at the *thresholded* decision level, many perturbations did not change the binary decision for a given patient and therefore produced near-zero Δ error; this should be interpreted as a property of discrete clinical decision-making (decision “flips” are required to change error) rather than as an absence of informative signal.

For interpretability, we summarized importance within clinically grounded kinematic families (baseline posture, sustained bias, excursions, variability, rhythmicity, and directionality) (**Figure 5A**) and across coarse anatomical regions (**Figure 5B**) (cranial, upper limb/proximal, lower limb/distal). Across phenotypes, importance concentrated in descriptors capturing baseline/sustained displacement and extreme excursions, whereas spectral and higher-order descriptors contributed more selectively. Here, “higher-order” features mainly comprised distributional and complexity measures (e.g., skewness/kurtosis, entropy-based measures including permutation entropy, and fractal-like complexity via Higuchi fractal dimension), which tended to refine decisions rather than drive them. Anatomically, influential descriptors frequently involved cranial and proximal upper-limb landmarks, consistent with their robust visibility in standard clinical videos and their sensitivity to axial/postural adjustments. Lower-limb descriptors contributed more variably: they were prominent for phenotypes with stereotyped limb patterning, and they may also become important in patients with generalized involvement (e.g., generalized dystonia), although their contribution is

inherently dependent on task, camera framing, and the captured field of view.

Despite shared global trends, each symptom exhibited a distinct importance profile aligned with clinical phenomenology. Dystonia was predominantly driven by baseline and sustained postural descriptors, consistent with tonic component and abnormal postures; excursion-type descriptors were secondary, compatible with phasic dystonic component superimposed on a tonic bias. The dominant topographic contribution arose from cranial/cervical and proximal upper-limb landmarks, reflecting clinically salient axial components, frequent involvement of axial and upper body segments in adulthood dystonia and compensatory upper-body adjustments; in generalized cases, lower-limb descriptors may also reasonably contribute when adequately captured. Tremor relied primarily on baseline/sustained displacement and overall movement burden rather than on a narrow spectral signature. While rhythmicity-related descriptors (FFT peak frequency/amplitude) were present, decision-level attribution suggested that tremor detection in this dataset was largely mediated through posture-linked oscillatory load and sustained variability, which is clinically plausible in a heterogeneous tremor population (including dystonic tremor), where frequency can vary across individuals, tasks, and recording conditions and where short windows can yield unstable single-peak spectral estimates. Myoclonus showed an event-like signature dominated by paroxysmal excursions (extreme minima/maxima and related excursion proxies), consistent with brief jerks producing disproportionate extremes in displacement time series; baseline descriptors contributed secondarily, plausibly reflecting jerks superimposed on a moving postural set-point. Athetosis was distinguished by a comparatively stronger contribution from directionality-related descriptors (e.g., repeated reversals captured by derivative sign changes and trajectory evolution proxies), consistent with slow, writhing movement characterized by continuously evolving trajectories rather than periodic oscillation or isolated paroxysms events. Stereotypies exhibited a predominantly segmental signature with comparatively greater limb (including lower-limb) involvement than most other phenotypes, consistent with repeated patterned actions that preserve a characteristic set-point while producing reproducible excursions; clinically, this limb-weighted profile may also help separate stereotypies from tics, which can involve variable distributions and “in many much more fashions ways” across body regions. For rarer phenotypes, we observed plausible but less stable signatures. Chorea, ballismus, and tics tended to be driven by excursion- and variability-related descriptors, consistent with irregular, abrupt and/or large-amplitude deviations, but these attributions should be interpreted cautiously given lower prevalence and higher sensitivity to fold composition.

Aggregating decision-level feature importance into clinically grounded kinematic families revealed structured overlaps between phenotypes that mirror bedside phenomenology and highlight plausible sources of diagnostic ambiguity. First, dystonia and tremor shared a strong reliance on baseline and sustained postural signals, consistent with the clinical observation that tremor often occurs on top of an abnormal postural set-point and that axial/proximal adjustments can dominate the video signature. In this context, tremor was differentiated primarily by a greater relative contribution of movement-burden descriptors (including segmental upper-limb contributors), whereas dystonia remained more strongly anchored in sustained postural bias. Second, we observed a partial overlap between myoclonus and tremor, driven by shared reliance on cranial/proximal descriptors capturing overall displacement burden. Clinically, this overlap is expected because both phenotypes can increase positional variability and intermittently produce excursions in standard video recordings; however, the relative weighting differed, with myoclonus exhibiting a more event-like profile dominated by extreme excursions (brief jerks) and tremor relying more on sustained oscillatory load (a more continuous movement pattern). Third, event-dominated phenotypes (tics, ballismus, and to some extent chorea) showed convergent importance patterns characterized by excursion- and variability-related evidence, consistent with abrupt, irregular and/or large-amplitude deviations, albeit with the above prevalence-related caveats. In contrast, athetosis emerged as the phenotype

most enriched for directionality-related evidence, supporting its differentiation from both oscillatory and purely paroxysmal phenomena. Overall, these overlap patterns suggest that the model organizes hyperkinetic disorders along a clinically meaningful kinematic continuum, ranging from sustained postural bias, through rhythmic movement burden, to paroxysmal excursions and directionality, while preserving phenotype-specific signatures at the decision level.

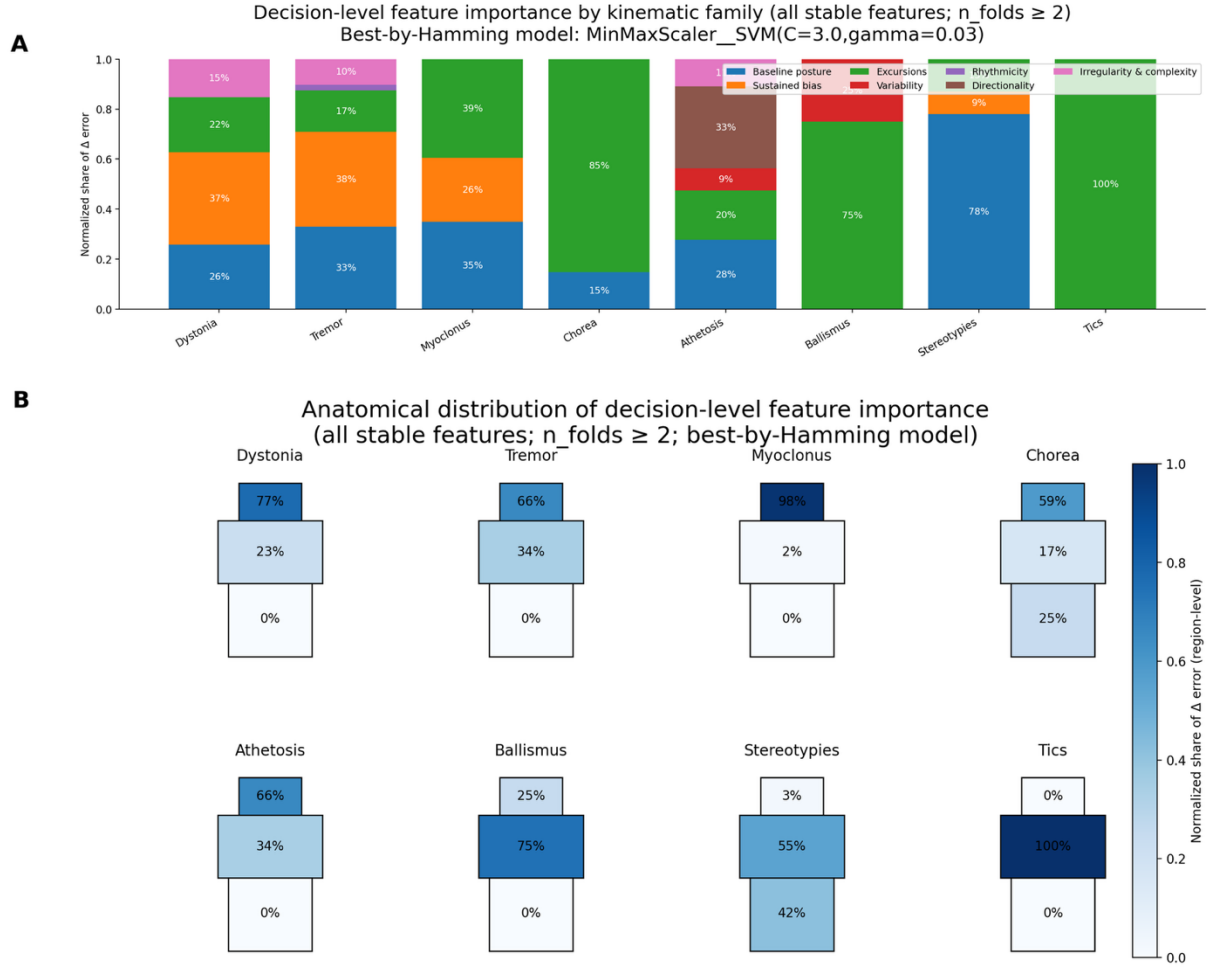


Figure 5. Clinically interpretable decision-level feature importance at the patient level. (A) Decision-level feature importance by kinematic family. Patient-level permutation importance was computed exclusively on the held-out outer test folds ($n_{\text{folds}} \geq 2$ stability criterion) and summarized for the best-by-Hamming model (MinMaxScaler + SVM, $C=3.0, \gamma=0.03$). Importance was defined as the increase in patient-level decision error induced by permuting one feature at a time, expressed as Δ error where $\text{error} = (\text{FP}+\text{FN})/N$ patients, while preserving the full inference pathway (window-level probabilities, p90 patient aggregation, and label-specific clinical thresholding). Bars report the normalized share of Δ error attributed to each clinically grounded kinematic family (baseline posture, sustained bias, excursions, variability, rhythmicity, directionality, and irregularity/complexity), with percentages indicating each family's contribution within symptom. Across phenotypes, importance concentrates in postural set-point descriptors (baseline posture and sustained bias) and extreme excursions, whereas rhythmicity and irregularity/complexity contribute more selectively, consistent with phenotype-specific motor phenomenology. (B) Anatomical distribution of decision-level importance. The same stable, decision-level attributions were aggregated by landmark region (head/face, upper limb, lower limb) and displayed as the normalized share of Δ error per symptom (color intensity and in-panel percentages). Head/face and proximal upper-limb descriptors account for the majority of decision-level evidence for several phenotypes, consistent with robust visibility and tracking of axial/proximal landmarks in standard clinical videos. Lower-limb contributions are more phenotype-dependent, increasing for selected phenotypes, consistent with task- and field-of-view-dependent expression of discriminative movement patterns.

Multi-Symptom Temporal Detection in Hyperkinetic Movement Disorders: Patient Level Example

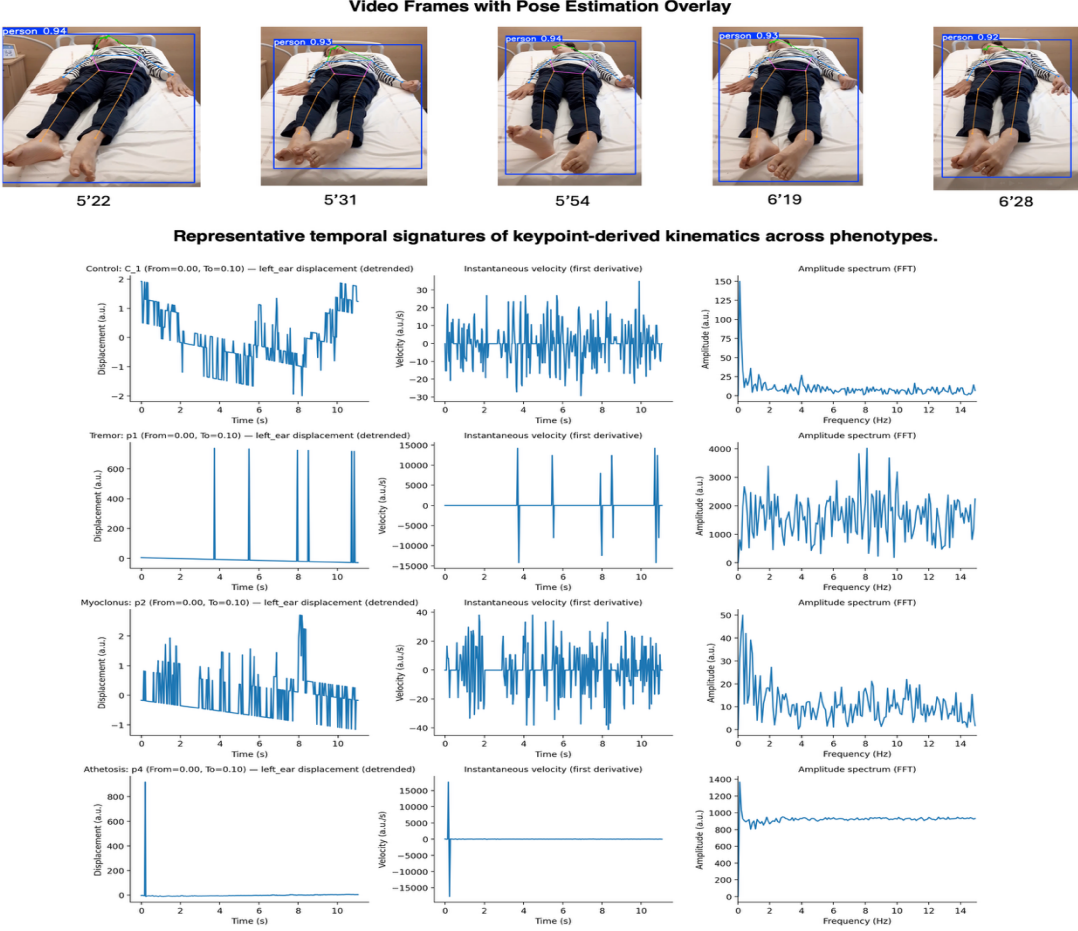


Figure 6. Illustrative frames with YOLOv8-based pose estimation (top) and representative temporal signatures of keypoint-derived kinematics across phenotypes (bottom). For each example (one control and three illustrative phenotypes), we display a detrended displacement trace from a head/face keypoint distance (left column), its instantaneous velocity (first derivative; middle), and the corresponding amplitude spectrum (FFT; right) computed over the same time window. Control traces show low-amplitude fluctuations and broadly distributed spectral energy without dominant structure. Tremor exhibits a more sustained oscillatory movement burden, expressed primarily as increased displacement variability and repeated velocity alternations; frequency structure may be present but is not necessarily dominated by a single stable peak under short windows and heterogeneous acquisition conditions, consistent with decision-level attribution relying more on global movement burden than on narrow-band spectral descriptors. Myoclonus demonstrates a paroxysmal, event-like pattern characterized by abrupt, high-amplitude excursions and sharp velocity spikes, consistent with the predominance of extreme-value (min/max) descriptors in patient-level importance. Athetosis shows slower, continuously evolving fluctuations with frequent directional changes and intermittent accelerations, compatible with a greater relative contribution of trajectory-evolution descriptors (directionality) rather than purely rhythmic signatures. Together, these representative traces provide an intuitive mapping from clinical phenomenology to the kinematic families used for interpretability (baseline/sustained displacement, excursions, variability, rhythmicity, and directionality).

4 Discussion

We developed a pose-based deep learning framework for automatic detection of hyperkinetic movement disorders (HMDs) from outpatient videos, an accessible and convenient alternative to sensor-based assessments^{44,45}. Previous applications explored detection, classification⁴⁶, and quantifi-

cation of various movement disorders, including mainly Parkinson’s disease ⁴⁷, gait disorders ⁴⁶, ataxia ⁴⁸, and tics ²⁶. Our approach uses deep learning primarily for robust 2D pose estimation, while clinically interpretable classification is driven by engineered time-series descriptors extracted from keypoint trajectories. Representing movement as sequences of anatomically meaningful landmarks allows us to quantify deviations in movement trajectories and localize the body regions at which “aberration” occur ⁸. Building on this representation, we structured analyses across several clinically relevant levels: (i) window-level screening of individual HMD expression versus normative control movement, (ii) multi-label detection to reflect simultaneous co-occurrence of multiple hyperkinetic phenomenologies within the same patient, (iii) patient-level inference obtained by aggregating repeated short observations into a consolidated phenotype profile, and (iv) decision-level feature-importance analyses to identify the kinematic families and anatomical regions most influential for patient-level clinical calls. Within this framework, we contrasted baseline sequential approaches on raw trajectories with an optimized pipeline that integrates robust feature engineering, scaling and calibration, model selection, and clinically motivated aggregation and thresholding. This design addresses a common clinical reality, many diseases to few phenotypes ⁴⁹, and supports translational potential ^{30 50} for objective indexing, monitoring, and trial-ready phenotyping in combined movement disorders.

No single metric captures all desirable properties of a clinical decision tool. Several performance measures are typically reported, yet they are not always intuitive for clinicians ⁵¹. We therefore interpret the evaluation landscape in terms that map to clinical intent. Sensitivity reflects how often the model identifies a phenotype when it is present (avoiding missed cases), while specificity reflects how often it correctly rejects the phenotype when absent (reducing false alarms). Precision indicates the trustworthiness of a positive call, and F1-score balances missed detections and over-calling. Importantly, in screening-like settings, the clinical cost of false alarms can be substantial, particularly when an automated system is intended to triage or trigger additional review. In our window-based analyses, the negative class was deliberately defined conservatively as control windows rather than symptom-absent windows from patients, so performance should be interpreted as discrimination between clinically labeled symptom expression and normative movement patterns, not as “symptom absence within patients” detection. Within this screening-oriented definition, patient-level aggregation yielded consistently high control specificity (1.00 across symptoms and raters once window evidence was pooled), indicating that repeated short observations rarely led to symptomatic labeling in healthy controls. This behavior is clinically desirable and suggests that pose-derived features capture stable normative movement signatures that are not easily misclassified as hyperkinetic activity when evidence is aggregated.

Window-level discrimination varied by phenotype, mirroring differences in movement phenomenology and the ease of defining symptom boundaries on routine videos. Dystonia, chorea, tremor and tics showed robust window-level reliability (positive-class F1 values in the ~0.8–0.9 range across raters) and strong subject identification after aggregation, consistent with relatively distinctive kinematic signatures: sustained abnormal posturing for dystonia, irregular purposeless excursions for chorea, oscillatory structure for tremor, and brief stereotyped bursts for tics. In contrast, athetosis, stereotypies, myoclonus and ballismus were more challenging at the 10-second scale, consistent with (i) slow, continuous, and often mixed-pattern movements (athetosis), (ii) heterogeneous, context-dependent repetitive behaviors (stereotypies), and (iii) highly intermittent, short-duration events that can be difficult to time-stamp consistently (myoclonus and ballismus). This pattern is reinforced by rater-dependence: tremor was highly concordant between annotation sets ($\Delta F1 \approx 0.01$), while myoclonus showed marked annotation-set dependence ($\Delta F1 \approx 0.32$), underscoring the clinical difficulty of time-stamping brief shock-like events and the sensitivity of learned signatures to labeling policy. Importantly, subject-level identification generally exceeded

window-level reliability, supporting the clinical utility of aggregating repeated short observations: majority-vote consolidation reduces the influence of sporadic window-level errors and recapitulates the clinical process of forming a judgement after reviewing multiple epochs rather than relying on a single short clip.

Under standardized examination conditions (rest, posture maintenance, action), symptom-versus-control separation for dystonia and tremor remained strong across several model families, with multiple pipelines reaching near-ceiling performance across conditions. These results are clinically consistent with the structured nature of standardized tasks and support context robustness, but they should be interpreted cautiously given the smaller condition-specific subsets. Together, they motivate prospective validation in larger cohorts and more naturalistic settings, where variability in filming geometry, clothing, occlusion, and task compliance is expected to increase.

Because clinical assessment frequently involves concurrent hyperkinetic phenotypes, we next asked whether pose-derived kinematic features can support simultaneous and clinically interpretable multi-label inference at the patient level. To reduce idiosyncratic rater effects, these analyses were conducted on a consensus dataset in which window-level annotations were harmonized across clinicians, anchoring evaluation to a shared clinical ground truth. Patient-level multi-label profiles were derived from window probabilities using robust p90 pooling followed by label-wise thresholding tuned exclusively on training subjects under a control-aware operating regime. At the patient level, discrimination was strong when probabilities were interpreted as ranked evidence rather than hard calls (macro-AUPRC 0.821 ± 0.019 ; macro-AUC 0.830 ± 0.029), indicating robust separability of symptomatic and asymptomatic individuals across cross-validation folds. Importantly, optimizing for different clinical priorities produced the expected trade-offs: maximizing correctness of the full patient-label decision set (best Hamming accuracy) yielded 0.764 ± 0.041 , whereas operating points designed to reduce clinical burden (lowest clinical cost) shifted decisions toward more conservative calling, consistent with how thresholds might be adapted to different workflows (screening-like sensitivity versus rule-in-like specificity). This “phenotype-specific operating landscape” is a critical clinical message: the same probabilistic backbone can be tuned to match the intended context of use rather than forcing a single operating point across all phenotypes.

To contextualize aggregate metrics, we examined best per-label models (selected to minimize patient-level errors) and decomposed predictions into true negatives, true positives, false positives and false negatives. Across 200 patient-label decisions (25 subjects \times 8 labels), per-label selection produced 28 total errors (86.0% correct decisions) with clinically interpretable error modes. Performance was strongest for phenotypes with distinctive and/or consistently annotated patterns: tics were perfectly identified in this cohort (TP=3, TN=22; no false positives or false negatives), and dystonia showed high sensitivity with only a single missed case (TP=20, FN=1) and minimal over-calling (FP=1). Myoclonus and chorea also showed high recall in this cohort (no false negatives), with remaining errors dominated by false positives, an error profile that, in practice, would often be triaged by clinical context and may be reduced by stricter operating points when false alarms are costly. In contrast, tremor carried the largest residual error burden (FN=4, FP=4), consistent with borderline presentations, task dependence, and overlap with non-specific movement patterns captured in short windows; athetosis similarly exhibited balanced false negatives and false positives (FN=2, FP=3), suggesting that subtle low-frequency fluctuations remain difficult to consolidate into an unambiguous patient-level call from brief windows alone. For rare labels, the decomposition was particularly informative: ballismus, observed in only three positive subjects, maintained perfect specificity (FP=0) but lower sensitivity (FN=2), illustrating cautious detection in the low-prevalence regime, avoiding overcalling a high-impact diagnosis at the expense of missed cases. Collectively, these findings support the feasibility of clinically constrained multi-label inference from pose-derived features while identifying, in a clinically actionable manner, where additional

data density and refined labeling are most likely to yield further gains.

A core methodological and clinical challenge in this domain is that no absolute ground truth exists for HMD classification. As highlighted in the literature, rated tasks are vulnerable to uncertainty and inter-rater variability ⁵². Consequently, some apparent model “errors” may reflect ambiguous or borderline phenomenology rather than purely algorithmic failure; in practice, a discordant prediction can sometimes flag a segment where the reference label itself is contestable, particularly for brief, intermittent events and for phenotypes with overlapping kinematic signatures. Majority voting can provide a pragmatic pseudo-ground truth at the patient level, but it has caveats, especially when disagreement reflects true ambiguity rather than noise. Models trained on assessments from multiple assessors could potentially outperform any individual assessors in specific settings ⁴⁶, but realizing this advantage will require explicit uncertainty-aware labeling (probabilistic labels, adjudication, or structured disagreement modeling) rather than excluding ambiguous cases. This issue becomes even more critical when moving from classification to quantification, where disagreement typically increases and clinical consequences of misestimation may be higher. Most current DL-based quantification work focuses on individual Parkinson’s disease symptoms such as levodopa-induced dyskinesia (LID) ⁵³, tremor, rising from a chair ⁵⁴, and in the hyperkinetic domain has addressed eye tics ²⁶, action myoclonus ⁵⁵ and focal dystonia ⁵⁶; quantification of multiple HMDs remains a key next step for the field and is the focus of our ongoing work.

Our decision-level feature-importance analyses provide a clinically grounded explanation for why the optimized models succeed and where they struggle. Importance was quantified at the patient decision level on held-out outer test folds only, aligned with the full inference pathway (window probabilities → p90 aggregation → label-specific thresholds), thereby avoiding information leakage and directly attributing the evidence that flips clinical decisions. Across phenotypes, decision-level importance concentrated in kinematic families capturing baseline posture and sustained displacement as well as extreme excursions and variability, whereas rhythmicity and higher-order irregularity/complexity descriptors contributed more selectively. This pattern supports a clinically intuitive interpretation: the models largely rely on descriptors that correspond to what clinicians observe at the bedside, movement burden, dispersion around a postural set-point, and episodic departures, while using spectral and complexity cues to refine decisions when physiology predicts them. Importances also revealed meaningful phenotype-specific profiles: dystonia and tremor were strongly shaped by baseline and sustained postural descriptors, consistent with tonic deviation and oscillatory load on top of a postural set-point; chorea and tics were dominated by excursion-type evidence, consistent with irregular, abrupt deviations; myoclonus showed an event-like profile driven by excursion and baseline burden consistent with brief jerks that disproportionately influence extremes; and athetosis showed relatively greater contributions from directionality-related evidence, consistent with slow writhing trajectories characterized by continuous evolution and repeated reversals rather than periodic oscillation or isolated paroxysms. At the anatomical level, influential evidence frequently arose from cranial and proximal upper-limb landmarks, which are robustly visible in routine clinic videos and sensitive to axial and upper-body adjustments; lower-limb contributions were more phenotype-dependent, becoming prominent for stereotypies and for phenotypes where limb patterning is salient within the field of view. Importantly, these attribution landscapes also map expected sources of clinical ambiguity: phenotypes that share reliance on similar kinematic families (e.g., sustained postural signals versus event-like excursions) are precisely those that can be difficult to disentangle in short windows.

Several limitations temper generalization. First, the number of subjects is modest and phenotypes are imbalanced, which constrains robustness for underrepresented labels and increases estimator variance, especially for rare, episodic phenotypes. Second, data originate from a single center with structured filming geometry; domain shift is expected with different cameras, distances,

clothing, occlusion, and examination styles. Third, the fixed 10-second window is a deliberate compromise: it enables stable statistical and spectral descriptors but can dilute very transient events and may broaden narrowband signatures. Adaptive or shorter windowing, or event-triggered segmentation, may better capture brief phenomena such as tics, isolated myoclonic jerks, or ballistic events. Fourth, inter-rater differences remain a central source of label noise; while our design mitigates leakage and supports consensus labeling, uncertainty-aware strategies would better reflect the absence of a gold standard, and excluding uncertain windows may underestimate real-world ambiguity. Fifth, our representation is based on 2D pose; axial rotations and subtle distal (hands) or facial signs may benefit from 3D pose, multimodal inputs, or specialized hand/facial tracking, particularly for subtle phenotypes such as tremor, myoclonus, and athetosis. Sixth, broader and more diverse control cohorts are needed to strengthen specificity estimates and calibrate thresholds under wider real-world variability. As with many healthcare AI studies, rigorous analytical standards remain essential; we aligned our reporting with TRIPOD recommendations ^{57,58} and the 2024 update ⁵⁹, but external validation remains necessary to establish clinical readiness.

We foresee three priorities. First, external multicenter prospective validation with diverse cameras, protocols, ages (including pediatrics), and genetically defined cohorts is required to quantify domain shift, calibrate thresholds, and establish generalizability. Second, temporal modeling that captures cross-window dependencies, symptom onset/offset, and amplitude modulation could improve stability while retaining interpretability, particularly for intermittent phenotypes. Third, workflow integration and governance will be essential, including privacy-preserving on-device processing, real-time feedback during structured exams, and human-in-the-loop review with versioned model cards and bias audits. Two additional methodological directions are especially relevant for combined HMDs. Symptom-specific modeling, one model per phenotype rather than a single monolithic model, appears aligned with both feature signatures and clinical reasoning, and may better accommodate phenotype-specific prevalence, ambiguity, and risk profiles. In addition, generative approaches may support future work by improving representation learning, uncertainty modeling, and data augmentation in limited sample regimes, but they must be validated carefully to ensure clinical plausibility and to avoid amplifying label noise.

Movement disorder specialists may perceive computer vision tools as potentially undermining core roles that depend on visual expertise and interpersonal assessment. The method we propose should be used to enhance clinical availability rather than replace clinician capabilities by supporting objective indexing of HMDs and their associations at a temporal granularity unreachable in routine practice. Automated, vision-based systems may enable more frequent self-assessments from home relayed to clinicians for improved therapeutic adjustments in fluctuating neurological conditions including hyperkinetic movement disorders ⁶⁰. Finally, computer vision technologies require maintenance of scientific, clinical, and ethical standards ensured by close collaboration between clinicians, data scientists, and patients. Diversity in datasets, including edge cases, is mandatory for robust generalization ⁴⁶, and will be best achieved through multicenter collaboration and data sharing.

5 Conclusion

Our pose-based framework represents a step toward automated, clinically interpretable detection of hyperkinetic movement disorder (HMD) phenomenology from routine outpatient videos. Deep learning is used to robustly estimate 2D keypoints, while classification is driven by transparent time-series descriptors extracted from anatomically meaningful trajectories. In a screening-oriented window-level setting against healthy controls, aggregation of repeated 10-s observations yields

highly conservative behavior in controls and improves subject identification despite phenotype-dependent variability at the window scale. At the patient level, consensus-labeled multi-label inference, implemented through robust p90 pooling of window probabilities and label-wise thresholds tuned on training subjects under a control-aware operating regime, achieves strong discrimination and exposes predictable trade-offs between sensitivity-oriented screening and more conservative rule-in behavior. Decision-level feature-importance analyses further show that patient-level calls are primarily supported by displacement-based evidence, with selective contributions from rhythmicity and higher-order irregularity/complexity descriptors, and anatomically plausible emphasis on cranial and proximal upper-limb landmarks. Together, these findings support the feasibility of scalable, objective, and explainable video-based phenotyping for complex and co-occurring HMDs, and motivate multicenter prospective validation, uncertainty-aware labeling, and enhanced temporal modeling to enable deployment as clinically governed decision support for diagnosis, monitoring, and therapeutic evaluation.

6 References

1. O’Shea, S. A. & Shih, L. C. Global Epidemiology of Movement Disorders: Rare or Underdiagnosed? *Semin. Neurol.* **43**, 004–016 (2023).
2. Pérez-Dueñas, B. *et al.* The Genetic Landscape of Complex Childhood-Onset Hyperkinetic Movement Disorders. *Mov. Disord.* **37**, 2197–2209 (2022).
3. Brandsma, R., Van Egmond, M. E., Tijssen, M. A. J., & the Groningen Movement Disorder Expertise Centre. Diagnostic approach to paediatric movement disorders: a clinical practice guide. *Dev. Med. Child Neurol.* **63**, 252–258 (2021).
4. Di Fonzo, A., Monfrini, E. & Erro, R. Genetics of Movement Disorders and the Practicing Clinician; Who and What to Test for? *Curr. Neurol. Neurosci. Rep.* **18**, (2018).
5. Lange, L. M. *et al.* Nomenclature of Genetic Movement Disorders: Recommendations of the International Parkinson and Movement Disorder Society Task Force - An Update. *Mov. Disord. Off. J. Mov. Disord. Soc.* **37**, 905–935 (2022).
6. Elble, R. J. & Ondo, W. Tremor rating scales and laboratory tools for assessing tremor. *J. Neurol. Sci.* **435**, 120202 (2022).
7. Tarakad, A. Clinical Rating Scales and Quantitative Assessments of Movement Disorders. *Neurol. Clin.* **38**, 231–254 (2020).
8. Tang, W., Van Ooijen, P. M. A., Sival, D. A. & Maurits, N. M. Automatic two-dimensional & three-dimensional video analysis with deep learning for movement disorders: A systematic review. *Artif. Intell. Med.* **156**, 102952 (2024).
9. Darling, A. *et al.* Clinical rating scale for pantothenate kinase-associated neurodegeneration: A pilot study. *Mov. Disord.* **32**, 1620–1630 (2017).
10. Domínguez-Carral, J. *et al.* Severity of *GNAO1* -Related Disorder Correlates with Changes in G-Protein Function. *Ann. Neurol.* **94**, 987–1004 (2023).
11. Haberfehlner, H. *et al.* Towards automated video-based assessment of dystonia in dyskinetic cerebral palsy: A novel approach using markerless motion tracking and machine learning. *Front. Robot. AI* **10**, (2023).
12. Vasques, X., Paik, H. & Cif, L. Application of quantum machine learning using quantum kernel algorithms on multiclass neuron M-type classification. *Sci. Rep.* **13**, 11541 (2023).
13. Friedrich, M. U., Relton, S., Wong, D. & Alty, J. Computer Vision in Clinical Neurology: A Review. *JAMA Neurol.* **82**, 407 (2025).

14. Martínez-García-Peña, R., Koens, L. H., Azzopardi, G. & Tijssen, M. A. J. Video-Based Data-Driven Models for Diagnosing Movement Disorders: Review and Future Directions. *Mov. Disord.* **40**, 2046–2066 (2025).
15. Gong, W. *et al.* Human Pose Estimation from Monocular Images: A Comprehensive Survey. *Sensors* **16**, 1966 (2016).
16. LeCun, Y., Bengio, Y. & Hinton, G. Deep learning. *Nature* **521**, 436–444 (2015).
17. Redmon, J., Divvala, S., Girshick, R. & Farhadi, A. You Only Look Once: Unified, Real-Time Object Detection. in *2016 IEEE Conference on Computer Vision and Pattern Recognition (CVPR)* 779–788 (IEEE, Las Vegas, NV, USA, 2016). doi:10.1109/CVPR.2016.91.
18. Pedregosa, F. *et al.* Scikit-learn: Machine Learning in Python. <https://doi.org/10.48550/ARXIV.1201.0490> (2012) doi:10.48550/ARXIV.1201.0490.
19. Chen, T. & Guestrin, C. XGBoost: A Scalable Tree Boosting System. in *Proceedings of the 22nd ACM SIGKDD International Conference on Knowledge Discovery and Data Mining* 785–794 (ACM, San Francisco California USA, 2016). doi:10.1145/2939672.2939785.
20. Breiman, L. Random Forests. *Mach. Learn.* **45**, 5–32 (2001).
21. Chawla, N. V., Bowyer, K. W., Hall, L. O. & Kegelmeyer, W. P. SMOTE: Synthetic Minority Over-sampling Technique. *J. Artif. Intell. Res.* **16**, 321–357 (2002).
22. Silva De Lima, A. L. *et al.* Freezing of gait and fall detection in Parkinson’s disease using wearable sensors: a systematic review. *J. Neurol.* **264**, 1642–1654 (2017).
23. Rupprechter, S. *et al.* A Clinically Interpretable Computer-Vision Based Method for Quantifying Gait in Parkinson’s Disease. *Sensors* **21**, 5437 (2021).
24. Bandt, C. & Pompe, B. Permutation Entropy: A Natural Complexity Measure for Time Series. *Phys. Rev. Lett.* **88**, 174102 (2002).
25. Delrobaei, M., Tran, S., Gilmore, G., McIsaac, K. & Jog, M. Characterization of multi-joint upper limb movements in a single task to assess bradykinesia. *J. Neurol. Sci.* **368**, 337–342 (2016).
26. Conelea, C. *et al.* Automated Quantification of Eye Tics Using Computer Vision and Deep Learning Techniques. *Mov. Disord.* **39**, 183–191 (2024).
27. Ali, M. M. & Mohamed, S. I. A pose estimation for motion tracking of infants cerebral palsy. *Multimed. Tools Appl.* **84**, 8261–8286 (2024).
28. Li, M. H., Mestre, T. A., Fox, S. H. & Taati, B. Vision-based assessment of parkinsonism and levodopa-induced dyskinesia with pose estimation. *J. NeuroEngineering Rehabil.* **15**, 97 (2018).
29. He, L., He, F., Li, Y., Xiong, X. & Zhang, J. A Robust Movement Quantification Algorithm of Hyperactivity Detection for ADHD Children Based on 3D Depth Images. *IEEE Trans. Image Process.* **31**, 5025–5037 (2022).
30. Van Der Stouwe, A. M. M. *et al.* Next move in movement disorders (NEMO): developing a computer-aided classification tool for hyperkinetic movement disorders. *BMJ Open* **11**, e055068 (2021).
31. Bradski, G. The OpenCV Library. *Dr Dobbs J. Softw. Tools* (2000).
32. Cao, Z., Hidalgo, G., Simon, T., Wei, S.-E. & Sheikh, Y. OpenPose: Realtime Multi-Person 2D Pose Estimation using Part Affinity Fields. Preprint at <https://doi.org/10.48550/ARXIV.1812.08008> (2018).
33. Pham, H. H., Khoudour, L., Crouzil, A., Zegers, P. & Velastin, S. A. Video-based Human Action Recognition using Deep Learning: A Review. Preprint at <https://doi.org/10.48550/ARXIV.2208.03775> (2022).
34. Jocher, G., Chaurasia, A. & Qiu, J. Ultralytics yolov8. 2023. (2024).
35. Mathis, A. *et al.* DeepLabCut: markerless pose estimation of user-defined body parts with deep learning. *Nat. Neurosci.* **21**, 1281–1289 (2018).
36. Harris, C. R. *et al.* Array programming with NumPy. *Nature* **585**, 357–362 (2020).

37. Virtanen, P. *et al.* SciPy 1.0: fundamental algorithms for scientific computing in Python. *Nat. Methods* **17**, 261–272 (2020).

38. McKinney, W. Data Structures for Statistical Computing in Python. in 56–61 (Austin, Texas, 2010). doi:10.25080/Majora-92bf1922-00a.

39. Bergstra, J. & Bengio, Y. Random Search for Hyper-Parameter Optimization. *J. Mach. Learn. Res.* **13**, 281–305 (2012).

40. Varoquaux, G. *et al.* Assessing and tuning brain decoders: Cross-validation, caveats, and guidelines. *NeuroImage* **145**, 166–179 (2017).

41. Sechidis, K., Tsoumakas, G. & Vlahavas, I. On the Stratification of Multi-label Data. in *Machine Learning and Knowledge Discovery in Databases* (eds Gunopulos, D., Hofmann, T., Malerba, D. & Vazirgiannis, M.) vol. 6913 145–158 (Springer Berlin Heidelberg, Berlin, Heidelberg, 2011).

42. Niculescu-Mizil, A. & Caruana, R. Predicting good probabilities with supervised learning. in *Proceedings of the 22nd international conference on Machine learning - ICML '05* 625–632 (ACM Press, Bonn, Germany, 2005). doi:10.1145/1102351.1102430.

43. Vasuques, X. *Machine Learning Theory and Applications: Hands-on Use Cases with Python on Classical and Quantum Machines*. (Wiley, Hoboken, New Jersey, 2024).

44. Longardner, K., Undurraga, F. V., Nahab, F. B., Hallett, M. & Haubenberger, D. How Do I Assess Tremor Using Novel Technology? *Mov. Disord. Clin. Pract.* **6**, 733–734 (2019).

45. Beuter, A., Legros, A., Cif, L. & Coubes, P. Quantifying Motion in Dystonic Syndromes: The Bare Essentials: *J. Clin. Neurophysiol.* **21**, 209–214 (2004).

46. Rupprechter, S. *et al.* A Clinically Interpretable Computer-Vision Based Method for Quantifying Gait in Parkinson's Disease. *Sensors* **21**, 5437 (2021).

47. Li, M. H., Mestre, T. A., Fox, S. H. & Taati, B. Automated vision-based analysis of levodopa-induced dyskinesia with deep learning. in *2017 39th Annual International Conference of the IEEE Engineering in Medicine and Biology Society (EMBC)* 3377–3380 (IEEE, Seogwipo, 2017). doi:10.1109/EMBC.2017.8037580.

48. Nunes, A. S. *et al.* Automatic Classification and Severity Estimation of Ataxia From Finger Tapping Videos. *Front. Neurol.* **12**, 795258 (2022).

49. Sadnicka, A. & Edwards, M. J. Between Nothing and Everything: Phenomenology in Movement Disorders. *Mov. Disord.* **38**, 1767–1773 (2023).

50. Lange, F. *et al.* Computer vision uncovers three fundamental dimensions of levodopa-responsive motor improvement in Parkinson's disease. *Npj Park. Dis.* **11**, 140 (2025).

51. Hicks, S. A. *et al.* On evaluation metrics for medical applications of artificial intelligence. *Sci. Rep.* **12**, 5979 (2022).

52. Lu, M. *et al.* Vision-Based Estimation of MDS-UPDRS Gait Scores for Assessing Parkinson's Disease Motor Severity. in *Medical Image Computing and Computer Assisted Intervention – MICCAI 2020* (eds Martel, A. L. *et al.*) vol. 12263 637–647 (Springer International Publishing, Cham, 2020).

53. Li, M. H., Mestre, T. A., Fox, S. H. & Taati, B. Automated assessment of levodopa-induced dyskinesia: Evaluating the responsiveness of video-based features. *Parkinsonism Relat. Disord.* **53**, 42–45 (2018).

54. Morinan, G. *et al.* Computer-vision based method for quantifying rising from chair in Parkinson's disease patients. *Intell.-Based Med.* **6**, 100046 (2022).

55. Hyppönen, J. *et al.* Automatic assessment of the myoclonus severity from videos recorded according to standardized Unified Myoclonus Rating Scale protocol and using human pose and body movement analysis. *Seizure* **76**, 72–78 (2020).

56. Zhang, Z. *et al.* Hold that pose: capturing cervical dystonia's head deviation severity from video. *Ann. Clin. Transl. Neurol.* **9**, 684–694 (2022).

57. Moons, K. G. M. *et al.* Transparent Reporting of a multivariable prediction model for Individual Prognosis Or Diagnosis (TRIPOD): Explanation and Elaboration. *Ann. Intern. Med.* **162**, W1–W73 (2015).

58. Collins, G. S., Reitsma, J. B., Altman, D. G. & Moons, K. G. M. Transparent Reporting of a multivariable prediction model for Individual Prognosis Or Diagnosis (TRIPOD): The TRIPOD Statement. *Ann. Intern. Med.* **162**, 55–63 (2015).

59. Collins, G. S. *et al.* TRIPOD+AI statement: updated guidance for reporting clinical prediction models that use regression or machine learning methods. *BMJ* e078378 (2024) doi:10.1136/bmj-2023-078378.

60. Dixon, T. C. *et al.* Movement-responsive deep brain stimulation for Parkinson's disease using a remotely optimized neural decoder. *Nat. Biomed. Eng.* <https://doi.org/10.1038/s41551-025-01438-0> (2025) doi:10.1038/s41551-025-01438-0.

6.1 Acknowledgements

The study was supported by a research grant from Dystonia Medical Research Foundation Canada (Registration Number 126616598 RR0001).

6.2 Author contributions

L.C.: Conceptualization; Methodology; Investigation; Assessment; Data Collection; Data Curation; Validation; Writing-Original Draft, Supervision; **D.D.:** Conceptualization; Investigation; Assessment; Data Collection; Writing-Review&Editing; **G.A.H.:** Conceptualization; Investigation; Assessment; Data Collection; Writing-Review&Editing; **J.D.O.E.:** Investigation; Assessment; Writing-Review&Editing; **N.D.:** Investigation; Assessment; Writing-Review&Editing; **M.C.J.:** Investigation; Assessment; Writing-Review&Editing; **C.H.:** Investigation; Assessment; Writing-Review&Editing; **T.W.:** Investigation; Assessment; Writing-Review&Editing; **G-M.H.:** Conceptualization; Investigation; Writing-Review&Editing; **S.Hu.:** Data Collection; Assessment; Writing-Review&Editing; **M.D.:** Data Collection; Assessment; Writing-Review&Editing; **Z.S.:** Assessment, Visualisation; Writing-Review&Editing; **M.M.U.R.:** Assessment, Visualisation; Writing-Review&Editing; **S.He.:** Assessment; Investigation; Writing-Review&Editing; **M.B.:** Methodology; Investigation; Data Curation; Writing-Review&Editing; **E.M.M.:** Methodology; Writing-Review&Editing; **J.B.:** Conceptualization; Writing-Review&Editing; **X.V.:** Conceptualization; Methodology; Investigation; Data Curation; Validation; Formal Analysis; Writing-Original Draft, Supervision.

6.3 Competing interests

This work was supported by a research grant from Dystonia Medical Research Foundation Canada (DMRFC), registration number 126616598 RR0001. D.D. received honoraria for expert opinion from TEVA. J.B. is shareholder of ONWARD Medical B.V., a company developing products for stimulation of the spinal cord, not related to this research. All other authors declare that they have no known competing financial interests or personal relationships that could have appeared to influence the work reported in this paper. Authors G.A.H., J.D.O.E., N.D., M.C.J., C.H., T.W., G-M.H., S.Hu., M.D., Z.S., M.M.U.R., M.B., E.M.M., and X.V. declare no financial or non-financial competing interests

6.4 Additional information

Supplementary information: The online version contains supplementary material available at <https://github.com/xaviersvasques/...> (data and code). Correspondence and requests for materials should be addressed to Laura Cif and Xavier Vasques.

Supplementary Material Methods

A Supplementary Material Methods

A.1 Video Processing and Feature Extraction Pipeline

A.1.1 Video decoding and temporal indexing

Let a clinical recording be a discrete video sequence $V = \{I_t\}_{t=1}^T$, where $I_t \in \mathbb{R}^{H \times W \times 3}$ is the RGB frame at index t , with frame height H , width W , and T total frames. Frames are decoded sequentially using OpenCV. The acquisition frame rate is read from the container metadata (FPS), and each frame is assigned a timestamp

$$\tau_t = \frac{\text{CAP_PROP_POS_MSEC}(t)}{1000} \text{ (seconds),}$$

providing the temporal alignment required for subsequent windowing and label synchronization.

A.1.2 2D pose estimation with YOLOv8x-pose-p6

For each frame I_t , we apply a pretrained YOLOv8 pose-estimation model (weights: `yolov8x-pose-p6.pt`) to infer a 2D human skeleton in a single forward pass. YOLOv8-Pose is a one-stage detector that outputs person detections and associated keypoints. In the COCO-keypoint convention, the model predicts $J = 17$ anatomical landmarks spanning face, upper limbs, trunk, and lower limbs (nose; left/right eye; left/right ear; left/right shoulder; left/right elbow; left/right wrist; left/right hip; left/right knee; left/right ankle).

Formally, for each detected subject k in frame t , the model outputs a set of normalized keypoints

$$\hat{\mathbf{p}}_{t,j}^{(k)} = (\hat{x}_{t,j}^{(k)}, \hat{y}_{t,j}^{(k)}), j \in \{1, \dots, J\},$$

where $\hat{x}, \hat{y} \in [0, 1]$ are expressed in image-normalized coordinates. In our implementation, we retain the first detected person in each frame (i.e., $k = 1$) to build a single, consistent pose time series per video.

Computation is executed on GPU (Google Colab).

A.1.3 Coordinate mapping to pixel space and structured storage

Normalized coordinates are converted to absolute pixel coordinates by scaling with the original frame dimensions:

$$x_{t,j} = \lfloor \hat{x}_{t,j} W \rfloor, y_{t,j} = \lfloor \hat{y}_{t,j} H \rfloor.$$

This preserves the native image scale and avoids distortions introduced by downstream resampling.

For each frame t , we store τ_t and the $2J$ pixel coordinates $\{x_{t,j}, y_{t,j}\}_{j=1}^J$ in a tabular structure (pandas DataFrame), yielding a per-video matrix of size $T \times (1 + 2J)$. If no pose is detected in a frame (or if keypoint extraction fails), the corresponding keypoint entries are set to missing values (NaN) rather than imputed at this stage; downstream steps handle missingness consistently within the ML pipeline (e.g., imputation inside cross-validation).

A.1.4 Per-frame displacement signals (radial image-plane magnitude)

In addition to raw keypoint coordinates, we compute a scalar displacement magnitude for each landmark at each frame. Using the image origin (0,0) as a fixed reference, the displacement signal for landmark j is

$$d_{t,j} = \sqrt{x_{t,j}^2 + y_{t,j}^2}.$$

This produces $J = 17$ landmark-specific displacement time series $\{d_{t,j}\}_{t=1}^T$, which serve as low-level motion signals for later windowed descriptor extraction. This representation is intentionally simple and robust: while it does not represent 3D biomechanics, it quantifies visible movement amplitude in the camera plane and preserves clinically meaningful segmental topography (distal vs proximal; cranial vs appendicular).

A.1.5 Quality-control artifact: annotated video export

For traceability and clinical QA, an annotated video is generated by overlaying the predicted skeleton on each frame and writing the resulting frames to an output video file. This provides a human-interpretable verification layer to detect failure modes (e.g., mis-detections, identity switches, occlusion-related dropouts) before feature engineering and model training. The output of the YOLO stage is therefore a temporally indexed pose time series per video:

1. timestamps τ_t ;
2. pixel-space keypoint trajectories $\{x_{t,j}, y_{t,j}\}$;
3. optional per-keypoint displacement magnitudes $\{d_{t,j}\}$;
4. an annotated video for visual QC.

These pose-derived signals and metadata constitute the input to the subsequent stages (windowing, derived descriptor computation, and machine-learning modeling).

A.2 Derived Additional Time-Series Features from landmark trajectories

A.2.1 Windowed landmark signals

For each video, YOLOv8-Pose provides 2D keypoint trajectories. From these trajectories, the pipeline constructs **per-landmark scalar displacement signals** (one signal per anatomical landmark) that quantify visible motion in the image plane and preserve segmental topography (e.g., distal vs proximal segments). Let $s_j(t)$ denote the displacement time series for landmark $j \in \{1, \dots, J\}$ at frame index t . Windows are defined by the expert annotation bounds (« From », « To ») in the exported spreadsheets and correspond to fixed-length segments (10 s in the main protocol). Within each window w , we therefore observe a sampled signal

$$\mathbf{s}_j^{(w)} = \{s_j(t)\}_{t=1}^{N_w},$$

with N_w frames and sampling frequency f_s (FPS; set to 30 Hz in the implementation). The feature extraction procedure operates independently on each window and each landmark signal.

A.2.2 Discrete derivatives and event-sensitive transforms

To capture temporal dynamics beyond amplitude, the method computes finite-difference derivatives within each window:

First difference (velocity proxy). With $s(t)$ denoting one landmark displacement signal within a window, the discrete first difference used in the code is

$$\Delta s(t) = s(t) - s(t-1), t = 2, \dots, N,$$

with $\Delta s(1) = 0$ implemented via a prepend convention.

Second difference magnitude (acceleration proxy). The “acceleration” surrogate is defined as the absolute second finite difference:

$$a(t) = |\Delta s(t) - \Delta s(t-1)|, t = 2, \dots, N,$$

again with a prepend convention for the initial value. This quantity is particularly sensitive to abrupt changes and jerk-like events.

A.2.3 Feature families and mathematical definitions (per landmark, per window)

For each landmark displacement signal $s(t)$ in a given window, a feature vector is computed comprising **distributional**, **temporal/kinematic**, **spectral**, and **nonlinear complexity** descriptors, plus short-horizon **rolling-mean** summaries. All features are computed directly from the windowed sample (no padding), and signals are cast to floating point; windows with fewer than two samples are skipped.

A.2.4 Distributional amplitude and shape descriptors

These quantify the “movement burden” and variability in a window.

- **Mean:** $\mu = \frac{1}{N} \sum_{t=1}^N s(t)$
- **Standard deviation:** $\sigma = \sqrt{\frac{1}{N} \sum_{t=1}^N (s(t) - \mu)^2}$
- **Variance:** $Var(s) = \sigma^2$
- **Median:** $median(s)$
- **Minimum / Maximum:** $\min_t s(t), \max_t s(t)$
- **Range (peak-to-peak):** $\max_t s(t) - \min_t s(t)$
- **Interquartile range (IQR):** $Q_{0.75}(s) - Q_{0.25}(s)$
- **Energy:** $E = \sum_{t=1}^N s(t)^2$

Additionally, two standardized shape moments are computed:

- **Skewness:** $\gamma_1 = \mathbb{E} \left[\left(\frac{s-\mu}{\sigma} \right)^3 \right]$ (sample estimate)
- **Excess kurtosis:** $\gamma_2 = \mathbb{E} \left[\left(\frac{s-\mu}{\sigma} \right)^4 \right] - 3$ (sample estimate)

These descriptors summarize baseline level, dispersion, and tail behavior (e.g., rare high-amplitude excursions).

A.2.5 Temporal evolution and direction-change proxies

These quantify slow drift and rapid alternations.

- **Linear trend (slope):** the slope of the least-squares fit

$$s(t) \approx \beta_0 + \beta_1 t, \text{ feature } = \beta_1.$$

- **Direction-change propensity (zero crossings of the first difference):** the number of sign reversals in $\Delta s(t)$, computed as

$$Z = \sum_{t=2}^{N-1} \mathbf{1}\{\Delta s(t) \cdot \Delta s(t+1) < 0\}.$$

This counts repeated alternations of movement direction in the displacement trajectory.

- **Mean absolute “acceleration”:**

$$\bar{a} = \frac{1}{N} \sum_{t=1}^N a(t),$$

where $a(t) = |\Delta s(t) - \Delta s(t-1)|$. This increases with abrupt changes and paroxysmal events.
combined_hmd

A.2.6 Spectral rhythmicity descriptors (FFT-based)

To quantify oscillatory structure, the pipeline computes the discrete Fourier transform of the windowed signal:

$$S(k) = \sum_{t=0}^{N-1} s(t) e^{-i2\pi kt/N}, k = 0, \dots, N-1.$$

Let $A(k) = |S(k)|$ be the magnitude spectrum, and let the corresponding frequency grid be

$$f(k) = \frac{k}{N} f_s \text{ (with negative-frequency wrap as in fftfreq).}$$

The method excludes the DC component $k = 0$ and finds the dominant oscillatory component via

$$k^* = \arg \max_{k \in \{1, \dots, N-1\}} A(k).$$

Two spectral features are retained:

- **Peak frequency:** $f_{\text{peak}} = f(k^*)$
- **Peak amplitude:** $A_{\text{peak}} = A(k^*)$

These are intended to capture rhythmic movement (e.g., tremor-like periodicity) while remaining lightweight and interpretable in short windows.

A.2.7 Entropy of amplitude distribution (histogram-based)

A Shannon entropy is computed from a fixed-bin histogram of the windowed samples. Let $\{b_m\}_{m=1}^{10}$ be 10 histogram bins over the observed range of $s(t)$, with density normalization. The method constructs a discrete distribution p_m (with a small ε added for numerical stability), then computes

$$H = - \sum_{m=1}^{10} p_m \log(p_m + \varepsilon).$$

This increases when the amplitude distribution is broader and less concentrated around a set-point.

A.2.8 Nonlinear irregularity / complexity descriptors

Two complementary measures are computed to characterize higher-order irregularity beyond variance or periodicity.

Higuchi fractal dimension (HFD). For each $k \in \{1, \dots, k_{\max}\}$ (with $k_{\max} = 5$), the algorithm forms k sub-series indexed by $m \in \{0, \dots, k-1\}$ and computes a length estimate $L_m(k)$ based on averaged absolute increments sampled every k points, with the normalization used in the implementation. The average length $L(k) = \frac{1}{k} \sum_m L_m(k)$ is then regressed in log–log space:

$$\log L(k) \approx c - D \log k,$$

and the feature returned is D (implemented as the negative slope of $\log L(k)$ vs $\log k$). Larger values indicate more scale-invariant irregularity in the trajectory.

Permutation entropy (PE). With embedding order $m = 3$ and delay $\tau = 1$, the method converts local length- m segments $(s(t), s(t+\tau), s(t+2\tau))$ into ordinal patterns (permutations) according to their rank order. Let $p(\pi)$ be the empirical probability of pattern π over the window. Permutation entropy is

$$PE = - \sum_{\pi} p(\pi) \log(p(\pi) + \varepsilon).$$

Higher PE corresponds to less predictable local ordering and greater temporal disorder.

A.2.9 Short-horizon rolling-mean summaries (sustained bias)

To separate sustained deviations from transient spikes, the pipeline computes centered rolling means with window sizes $w \in \{3, 5, 7\}$ frames:

$$r_w(t) = \frac{1}{|\mathcal{N}_w(t)|} \sum_{u \in \mathcal{N}_w(t)} s(u),$$

where $\mathcal{N}_w(t)$ is the centered neighborhood of width w (with edge handling via `min_periods = 1`). The exported feature is the average of $r_w(t)$ over time:

$$\bar{r}_w = \frac{1}{N} \sum_{t=1}^N r_w(t).$$

These descriptors emphasize persistent displacement within the window while reducing sensitivity to isolated artefacts.

A.2.10 Feature naming and dimensionality

Features are stored using a transparent naming convention combining the landmark displacement channel name (e.g., `right_wrist_distance`) and the descriptor suffix (e.g., `_fft_peak_freq`, `_higuchi_fd`). For each window and each landmark displacement signal, this implementation computes **19 primary descriptors** (distributional + temporal + spectral + entropy + complexity) and **3 rolling-mean descriptors**, yielding **22 features per landmark per window**. With $J = 17$ landmarks, this corresponds to $22 \times 17 = 374$ derived features per window in the multi-label pipeline.

A.3 Window-Based Binary Classification of Individual HMD Presence Versus Absence

This section describes the **binary, window-level screening pipeline** used to detect the presence of a single HMD phenotype in **10-second segments**, as implemented in `windows.py`.

A.3.1 Window definition, quality filtering, and label construction

For each recording (one subject per file), the pose-derived time series are already organized in a tabular structure containing (i) **keypoint displacement channels** (17 anatomical landmarks) and (ii) clinical annotation columns per phenotype. A **window** is defined by the pair $(From, To)$ and corresponds to a contiguous time interval of fixed duration (10 s in the study protocol). All samples belonging to the same $(From, To)$ pair form one group w .

Let $a_t^{(\ddagger)} \in \{0, 1, 2\}$ denote the rater-provided frame-level annotation for phenotype \ddagger at time index t within window w . The script enforces two key filtering rules before feature extraction:

1. **Uncertainty exclusion:** any window containing at least one uncertain label ($a_t^{(\ddagger)} = 2$) is removed:

$$w \text{ is valid} \iff \forall t \in w, a_t^{(\ddagger)} \neq 2.$$

2. **Completeness of pose-derived channels:** any window containing missing values in the displacement channels is removed.

After filtering, a **binary window label** is assigned using an “any-positive” rule:

$$y_w^{(\ddagger)} = \mathbb{1} \left[\exists t \in w \text{ such that } a_t^{(\ddagger)} = 1 \right].$$

This yields $y_w^{(\ddagger)} \in \{0, 1\}$ per window w and phenotype \ddagger .

A.3.2 Screening-oriented negative class (controls only)

The pipeline is explicitly configured as a **screening-style case-control contrast**: when a window is labeled negative ($y_w^{(\ddagger)} = 0$) and the recording belongs to a patient (i.e., not a control subject), that window is **excluded** from the dataset. Only **control** windows contribute to the negative class. Formally, if $g(w)$ denotes the subject identity for window w , and \mathcal{C} is the set of control subjects, then:

$$\text{keep } w \iff (y_w^{(\ddagger)} = 1) \vee (g(w) \in \mathcal{C}).$$

This design prevents “symptom-absent patient windows” from being used as negatives and forces the classifier to learn a discrimination between **symptom-expressing patient windows** (positives) and **healthy control windows** (negatives).

A.3.3 Feature representation per window

For each valid window w , the script extracts engineered descriptors from the 17 displacement channels (one per landmark), producing a fixed-dimensional vector $\mathbf{x}_w \in \mathbb{R}^d$. The feature extractor includes distributional statistics (mean, std, range, skewness, kurtosis, energy, IQR), temporal proxies (slope, zero-crossings, mean absolute second difference), spectral features (FFT peak frequency/amplitude), and nonlinear complexity metrics (Higuchi fractal dimension and permutation entropy), along with short-horizon rolling mean summaries.

The resulting dataset for phenotype \uparrow is:

$$\mathcal{D}^{(\uparrow)} = \left\{ \left(\mathbf{x}_w, y_w^{(\uparrow)}, g(w) \right) \right\}_{w=1}^N,$$

where $g(w)$ is the subject identifier (group label) used for leakage-free splitting.

A.3.4 Leakage-free cross-validation at the subject level

To prevent leakage between training and testing, the evaluation uses **StratifiedGroupKFold** (5 folds) with shuffling and a fixed random seed. The split produces indices $\mathcal{I}_{\text{train}}^{(k)}, \mathcal{I}_{\text{test}}^{(k)}$ such that:

$$g(w) \in \text{train fold} \Rightarrow g(w) \notin \text{test fold}$$

for every subject, while attempting to preserve the class ratio in each fold (stratification on y).

A.3.5 Training-time class balancing (within each fold)

Because the screening dataset may be imbalanced, the script applies a **fold-local undersampling heuristic** on the training windows. Let n_0 and n_1 be the counts of negative and positive training windows, respectively. If the relative imbalance exceeds 20%:

$$\frac{|n_0 - n_1|}{\max(n_0, n_1)} > 0.2,$$

the majority class is randomly resampled down to match the minority class count:

$$\mathcal{D}_{\text{train}}^{\text{bal}} = \text{Resample}(\mathcal{D}_{\text{train}}), n_0 \approx n_1.$$

This balancing is applied **only on the training partition** of each fold and never on the test set.

A.3.6 Preprocessing (scaling) and numeric stability

For each fold, a feature scaler $S(\cdot)$ is fit on the balanced training features and applied to both train and test features:

$$\tilde{\mathbf{x}} = S(\mathbf{x}).$$

The pipeline benchmarks several scalers (StandardScaler, MinMaxScaler, RobustScaler, PowerTransformer). After scaling, numerical stability is enforced by mapping NaNs and infinities to finite values (0 for NaN and bounded large magnitudes for $\pm\infty$).

A.3.7 Model families, hyperparameter enumeration, and probability calibration

For each phenotype \hat{y} , we benchmarked a set of representative classifier families. Each model defines a scoring function $f_\theta : \mathbb{R}^d \rightarrow \mathbb{R}$ (or directly a probability) applied to the window feature vector \mathbf{x}_w . When a calibrated probability was available, we denote

$$\hat{p}_w = \Pr_{\theta}(y_w^{(\hat{y})} = 1 \mid \mathbf{x}_w) \in [0, 1],$$

and use \hat{p}_w for ROC-AUC computation and thresholded predictions for F1/accuracy. All hyperparameters were explored via an explicit Cartesian product enumeration (scikit-learn ParameterGrid) and evaluated under subject-grouped cross-validation; performance was summarized by the mean of fold-wise metrics.

Gradient-boosted decision trees (XGBoost) We evaluated XGBoost gradient boosting over trees, where the model is an additive ensemble

$$f_\theta(\mathbf{x}) = \sum_{m=1}^M \eta h_m(\mathbf{x}),$$

with h_m decision trees and learning rate η . The tested hyperparameter grid was: number of trees $M \in \{100, 200, 300\}$, maximum depth $\in \{6\}$, learning rate $\in \{0.05, 0.1\}$, subsampling ratio $\in \{1.0\}$, column subsampling $\in \{1.0\}$, minimum child weight $\in \{1, 5\}$, and split loss regularization $\gamma \in \{0, 1\}$.

Gradient-boosted decision trees (LightGBM) We evaluated LightGBM, a histogram-based gradient boosting implementation. The tested grid was: number of trees $\in \{100, 200, 300\}$, number of leaves $\in \{31, 63\}$, learning rate $\in \{0.05, 0.1\}$, max depth $\in \{-1\}$ (unconstrained), feature fraction $\in \{1.0\}$, bagging fraction $\in \{1.0\}$, minimum child samples $\in \{10\}$, and ℓ_2 regularization $\lambda \in \{0.1, 1.0\}$.

Random Forests We evaluated RandomForest classifiers, i.e., bagged ensembles of decision trees:

$$\hat{p}(\mathbf{x}) = \frac{1}{M} \sum_{m=1}^M \hat{p}_m(\mathbf{x}),$$

where \hat{p}_m is the class probability from tree m . The tested grid was: number of trees $M \in \{100, 200, 300\}$, maximum depth $\in \{\text{None}\}$ (unconstrained), minimum samples to split $\in \{2\}$, minimum samples per leaf $\in \{1\}$, and feature subsampling rule $\in \{\text{sqrt}\}$.

Support Vector Machine (RBF kernel) We evaluated SVMs with a radial basis function kernel:

$$K(\mathbf{x}, \mathbf{x}') = \exp \left(-\gamma \|\mathbf{x} - \mathbf{x}'\|^2 \right),$$

with penalty parameter C . The grid was: $C \in \{1, 10\}$, kernel fixed to RBF, and $\gamma \in \{\text{scale}, 0.01\}$. Probabilistic outputs were enabled (probability=True) and further probability calibration was applied as described below.

Logistic Regression We evaluated ℓ_2 -regularized logistic regression, where

$$\hat{p}(\mathbf{x}) = \sigma(\mathbf{w}^\top \mathbf{x} + b), \sigma(z) = \frac{1}{1 + e^{-z}}.$$

The tested grid was: inverse regularization strength $C \in \{1\}$, penalty $\in \{\ell_2\}$, solver $\in \{\text{lbfgs}\}$, and maximum iterations $\in \{1000\}$.

k-Nearest Neighbors (KNN) We evaluated KNN with Euclidean distance ($p = 2$). For a query \mathbf{x} , predictions are derived from the label distribution among the k nearest training points. The grid was: $k \in \{5, 7\}$, weights $\in \{\text{uniform}\}$, Minkowski power $p \in \{2\}$.

Multi-Layer Perceptron (MLP) We evaluated a feedforward neural network classifier with ReLU nonlinearity. The grid was: hidden layer sizes $\in \{(128,), (64, 64)\}$, weight decay parameter $\alpha \in \{0.01, 0.0001\}$, activation $\in \{\text{relu}\}$, solver $\in \{\text{adam}\}$, initial learning rate $\in \{0.001\}$, and batch size $\in \{64\}$.

A.3.8 Probability calibration (applied to SVM and Random Forest variants)

To ensure well-behaved probabilistic outputs for ROC-AUC and downstream analyses, models in the SVM and RandomForest families were additionally wrapped in sigmoid calibration (CalibratedClassifierCV, 3-fold internal calibration). Concretely, for a base model score $f(\mathbf{x})$, calibrated probabilities are obtained via Platt scaling:

$$\hat{p}(\mathbf{x}) = \sigma(a f(\mathbf{x}) + b),$$

where a, b are learned on calibration folds. Calibration is performed strictly within each outer training fold to avoid test leakage.

Window-level evaluation metrics

Within each fold, the trained model produces:

- predicted labels $\hat{y}_w \in \{0, 1\}$,
- predicted probabilities $\hat{p}_w = \Pr(\hat{y}_w = 1)$.

The script reports per-fold:

- **F1-score** for class 1 and class 0 (from classification_report),

$$F1 = \frac{2 \cdot Precision \cdot Recall}{Precision + Recall},$$

- **Accuracy**,

$$Acc = \frac{1}{N} \sum_w \mathbb{1}[\hat{y}_w = y_w],$$

- **ROC-AUC** computed from \hat{p}_w .

Fold-level metrics are averaged across valid folds (folds lacking both classes are skipped to avoid degenerate AUC estimation).

Optional subject-level voting (derived from window predictions)

Although the primary task is window-level screening, the script also derives a **subject-level decision** by aggregating window predictions for each subject in the test folds.

For a subject g , let $\{\hat{y}_w\}_{w \in \mathcal{W}(g)}$ be the set of predicted window labels for that subject across test windows. The subject-level predicted label is computed by majority vote (equivalently, mean threshold at 0.5):

$$\hat{Y}_g = \mathbb{1} \left[\frac{1}{|\mathcal{W}(g)|} \sum_{w \in \mathcal{W}(g)} \hat{y}_w \geq 0.5 \right].$$

The subject-level “ground truth” is defined as:

$$Y_g = \mathbb{1} [\exists w \in \mathcal{W}(g) \text{ with } y_w = 1],$$

i.e., a subject is positive if any of their retained windows is positive. Subject-level accuracy, sensitivity, and specificity are then computed from (\hat{Y}_g, Y_g) across evaluated subjects.

A.4 Multi-label detection of concurrent HMD phenotypes

A.4.1 Problem formulation and data representation

Let L denote the number of HMD phenotypes (here $L = 8$). Each clinical video is partitioned into non-overlapping (annotation-defined) 10-s windows w , and each window is represented by a feature vector $\mathbf{x}_w \in \mathbb{R}^d$ computed from pose-derived kinematic descriptors. Each window carries a *multi-label* target vector

$$\mathbf{y}_w = (y_w^{(1)}, \dots, y_w^{(L)}) \in \{0, 1\}^L,$$

where $y_w^{(\dagger)} = 1$ indicates presence of phenotype \dagger in that window and 0 indicates absence. Windows with uncertain clinical annotation are excluded to preserve a strictly binary ground truth for supervised learning.

To reduce rater idiosyncrasies for the multi-label task, we conduct all multi-label analyses on a *consensus reference dataset* obtained by harmonizing the independent clinician ratings into a single window-level multi-label ground truth.

We retain control subjects and (optionally) symptom-absent windows (“all-zero” label vectors) to anchor the negative class with normative movement, which is critical for control-aware operating regimes and calibration of false-alarm constraints.

A.4.2 Patient-level grouping and leakage-free cross-validation

Windows are *not independent* because many windows belong to the same subject. We therefore enforce group-wise splitting by subject (patient/control identifier) to prevent train–test leakage.

Define a subject index mapping $g(w) \in \{1, \dots, N\}$ indicating the subject associated with window w . For subject s , define its aggregated (OR) label vector used for stratification:

$$\mathbf{Y}_s = \max_{w: g(w)=s} \mathbf{y}_w \text{ (element-wise OR across windows).}$$

Cross-validation partitions are generated at the subject level using multilabel-stratified K-fold splitting (preserving the joint prevalence structure across labels as much as possible), then expanded back to the corresponding window sets for model training and evaluation.

This ensures that no subject contributes windows to both training and test folds, and that prevalence of rare phenotypes is controlled at the subject level rather than at the window level (which would otherwise inflate effective sample size and bias estimates).

A.4.3 Multi-label learning strategy: binary relevance with calibrated probabilities

We implement multi-label prediction via **binary relevance**: one probabilistic binary classifier per label \uparrow , trained on all windows with that label's binary targets. Concretely, for each $\uparrow \in \{1, \dots, L\}$ we learn a scoring function $f_{\uparrow}(\mathbf{x})$ and an associated probability model

$$\hat{p}_w^{(\uparrow)} = \Pr(y_w^{(\uparrow)} = 1 \mid \mathbf{x}_w) \in [0, 1].$$

The window-level probability vector is $\hat{\mathbf{p}}_w = (\hat{p}_w^{(1)}, \dots, \hat{p}_w^{(L)})$.

Because several strong baselines (e.g., linear SVM variants) do not natively output calibrated probabilities, we apply explicit probability extraction rules: (i) use predict_proba when available; (ii) otherwise use calibrated decision scores via sigmoid calibration (CalibratedClassifierCV) when feasible; and (iii) fall back to a logistic mapping of the decision function,

$$\hat{p} = \sigma(z) = \frac{1}{1 + e^{-z}},$$

when calibration is not statistically feasible for rare labels (e.g., too few positives for K-fold calibration).

Per-label preprocessing, feature selection, and imbalance handling (within fold)

Within each outer training fold, each label-specific pipeline can include:

1. **Scaling/normalization** (label-agnostic transform but selected per candidate pipeline).
2. **Univariate feature selection** via mutual information: Select the top k features maximizing $I(X_j; y^{(\uparrow)})$, yielding a reduced vector $\tilde{\mathbf{x}}_w \in \mathbb{R}^{k_{\uparrow}}$. Label-specific k_{\uparrow} is allowed to reflect phenotype-dependent signal sparsity.
3. **Class rebalancing** through (optional) SMOTE variants restricted to the training fold only, with safeguards that adapt k -neighbors to the minority count and avoid synthetic sampling when infeasible.
4. **Class weighting** (e.g., balanced weights) to reduce bias toward the majority class when prevalence is low.

All of these operations are performed inside the training data of each fold to avoid leakage of distributional information from the test subjects.

A.4.4 From window probabilities to patient-level multi-label profiles

Clinical interpretation and downstream reporting are performed at the **patient level**, not at the window level, because clinical phenotyping is ultimately a subject-level decision (presence/absence of each phenotype for a patient). We therefore aggregate repeated short observations (10-s windows) into a patient-level probability vector.

For subject s , let $W_s = \{w : g(w) = s\}$ denote its set of windows, with cardinality $|W_s| = n_s$. For each label \uparrow , we aggregate the set $\{\hat{p}_w^{(\uparrow)} : w \in W_s\}$ into a patient-level probability $\hat{\pi}_s^{(\uparrow)}$ using one of the following operators:

Percentile pooling (p90; primary).

$$\hat{\pi}_s^{(\uparrow)} = \text{Quantile}_q(\{\hat{p}_w^{(\uparrow)}\}_{w \in W_s}), q = 0.90.$$

This implements a robust “high-evidence” summary: the patient-level score reflects the typical upper tail of window evidence rather than the single maximum (which can be unstable) or the mean (which can dilute intermittent phenomena).

For completeness, the pipeline also supports:

Max pooling: $\hat{\pi}_s^{(\uparrow)} = \max_{w \in W_s} \hat{p}_w^{(\uparrow)}$.

Top- k mean pooling: $\hat{\pi}_s^{(\uparrow)} = \frac{1}{k} \sum_{i \in \text{Top}k} \hat{p}_{w_i}^{(\uparrow)}$, where $\text{Top}k$ are the k largest window probabilities.

Noisy-OR pooling (event accumulation):

$$\hat{\pi}_s^{(\uparrow)} = 1 - \prod_{w \in W_s} (1 - \hat{p}_w^{(\uparrow)}),$$

which approximates the probability that *at least one* window contains the phenotype if window events are treated as conditionally independent given the model.

Ground-truth patient labels for evaluation are defined consistently as:

$$Y_s^{(\uparrow)} = \max_{w \in W_s} y_w^{(\uparrow)}.$$

A.4.5 Label-wise thresholding tuned on training subjects under control-aware constraints

Patient-level probabilities $\hat{\pi}_s$ are converted into binary patient-level calls via **label-specific thresholds** τ_{\uparrow} , chosen *exclusively on the training subjects* of each fold:

$$\hat{Y}_s^{(\uparrow)} = \mathbb{I}[\hat{\pi}_s^{(\uparrow)} \geq \tau_{\uparrow}].$$

Thresholds are optimized over a dense grid $\mathcal{T} \subset (0, 1)$ (e.g., 199 values between 0.01 and 0.99).

Crucially, threshold selection is **control-aware**. Let $\mathcal{S}_{\text{ctrl}}$ be the subset of control subjects in the training fold (identified by subject IDs), and \mathcal{S}_{all} all training subjects. For a candidate threshold t , define confusion counts on the training set:

$$\text{TN}(t), \text{FP}(t), \text{FN}(t), \text{TP}(t),$$

and corresponding rates:

$$\text{FPR}(t) = \frac{\text{FP}(t)}{\text{FP}(t) + \text{TN}(t)}, \text{FNR}(t) = \frac{\text{FN}(t)}{\text{FN}(t) + \text{TP}(t)}, \text{Spec}(t) = 1 - \text{FPR}(t), \text{Rec}(t) = 1 - \text{FNR}(t).$$

Additionally, compute **control-only** false positives $\text{FP}_{\text{ctrl}}(t)$ and $\text{FPR}_{\text{ctrl}}(t)$ restricted to $\mathcal{S}_{\text{ctrl}}$.

We support several threshold policies; the primary one is a **clinical-cost objective** with optional label-specific weighting:

$$\mathcal{C}_{\uparrow}(t) = (1 - \alpha_{\uparrow}) \text{FPR}_{\uparrow}(t) + \alpha_{\uparrow} \text{FNR}_{\uparrow}(t),$$

and we select

$$\tau_{\uparrow} = \arg \min_{t \in \mathcal{T} \cap \text{Feasible}_{\uparrow}} \mathcal{C}_{\uparrow}(t),$$

where $\alpha_{\uparrow} \in [0, 1]$ prioritizes false negatives ($\alpha_{\uparrow} \uparrow$) versus false positives ($\alpha_{\uparrow} \downarrow$). Feasibility enforces clinically motivated constraints, including: (i) maximum allowed number of control false positives, (ii) maximum control FPR, and/or (iii) minimum specificity targets, with label-specific targets permitted for rare/high-impact phenotypes.

This design yields phenotype-specific operating points aligned with clinical priorities (e.g., conservative behavior for rare labels, stricter control false-alarm limits for screening deployment).

A.4.6 Model selection: global comparators and per-label error-minimizing selection (optional nested layer)

Two complementary selection paradigms are used:

1. **Global pipeline selection** (single configuration across labels) based on a comparator metric (macro-AUPRC, macro-AUC, sample-wise Jaccard, Hamming accuracy, or a clinical-cost summary), computed at the patient level and averaged across folds.
2. **Per-label “best model” selection** (one pipeline per phenotype) that minimizes patient-level errors for that label. Concretely, for label \uparrow and candidate configuration c , compute the patient-level error rate

$$\text{Err}_{\uparrow}^{(c)} = \frac{\text{FP}_{\uparrow}^{(c)} + \text{FN}_{\uparrow}^{(c)}}{|\mathcal{S}|},$$

under the same aggregation (p90) and thresholding mechanism, and select the configuration achieving minimal $\text{Err}_{\uparrow}^{(c)}$ under the desired constraints.

In the implementation, this can be embedded in an inner (nested) cross-validation loop to prevent optimistic bias when selecting per-label models and thresholds.

A.4.7 Patient-level multi-label evaluation metrics

All primary metrics are computed at the **patient level** from \mathbf{Y}_s and $\hat{\mathbf{Y}}_s$, with discrimination metrics computed from $\hat{\pi}_s$:

- **Macro ROC-AUC** and **macro AUPRC** computed label-wise and averaged across labels, with “safe” handling that skips labels lacking both classes in a fold.
- **Micro-F1** and **macro-F1** on thresholded outputs.
- **Hamming loss**:

$$\text{HL} = \frac{1}{NL} \sum_{s=1}^N \sum_{\uparrow=1}^L \mathbb{I}[\hat{Y}_s^{(\uparrow)} \neq Y_s^{(\uparrow)}], \text{Hamming accuracy} = 1 - \text{HL}.$$

- **Sample-wise Jaccard index** averaged over subjects:

$$J = \frac{1}{N} \sum_{s=1}^N \frac{|\hat{\mathcal{L}}_s \cap \mathcal{L}_s|}{|\hat{\mathcal{L}}_s \cup \mathcal{L}_s|},$$

where $\mathcal{L}_s = \{\uparrow : Y_s^{(\uparrow)} = 1\}$ and $\hat{\mathcal{L}}_s = \{\uparrow : \hat{Y}_s^{(\uparrow)} = 1\}$.

- **Exact match ratio:** fraction of subjects with perfectly correct multi-label profiles $\hat{\mathbf{Y}}_s = \mathbf{Y}_s$.

Finally, because clinical deployment requires explicit false-alarm accounting in healthy individuals, we report **control-only** false positives and control FPR per label on held-out folds, in addition to overall specificity.

A.5 Features Importance

This section describes the feature-importance procedure implemented in `features.py`. The goal is to quantify, for each phenotype, **which engineered kinematic descriptors most strongly influence the final patient-level decision**, under the *exact same inference mechanism used in the main multi-label pipeline* (window probabilities → patient aggregation → label-wise thresholding).

What “importance” measures in our setting

Our deployed decision rule for a given label \uparrow is evaluated at the **patient level**. For patient s , we first compute window-level probabilities $\hat{p}_w^{(\uparrow)}$ for all windows $w \in W_s$, then aggregate them using percentile pooling (p90) to obtain a patient probability $\hat{\pi}_s^{(\uparrow)}$, and finally threshold:

$$\hat{\pi}_s^{(\uparrow)} = Q_{0.90}(\{\hat{p}_w^{(\uparrow)}\}_{w \in W_s}), \hat{Y}_s^{(\uparrow)} = \mathbb{1}[\hat{\pi}_s^{(\uparrow)} \geq \tau_{\uparrow}].$$

Feature importance is defined **with respect to the final patient-level classification error** produced by this full chain. Concretely, for each label \uparrow we use the patient-level error rate:

$$Err^{(\uparrow)} = \frac{FP^{(\uparrow)} + FN^{(\uparrow)}}{N_{\text{patients}}}.$$

This is a direct “how many patients are misclassified” objective, which is aligned with clinical deployment constraints and complements discrimination metrics (AUC/AUPRC).

Strict leakage avoidance: importance computed on outer test folds only

Feature importance is computed **only on held-out outer test folds**, never on training data. For each outer fold k :

1. Fit the complete label-specific pipeline on the **outer training windows** (including scaler, optional SelectKBest, optional SMOTE, classifier).
2. Tune label-wise patient thresholds τ_{\uparrow} **using only outer-training patients** (with control-aware constraints as configured).
3. Compute feature importance by permuting test-fold features and measuring the change in **patient-level error** on the same outer test patients.

This design ensures that both the model parameters and the thresholds are fixed **before** importance is measured, and that importance reflects genuine out-of-sample behavior.

Baseline patient-level predictions on the test fold

Fix one phenotype \uparrow and one outer fold k . Let $X_{\text{test}} \in \mathbb{R}^{n \times d}$ be the matrix of test windows (rows are windows; columns are features), $g \in \{1, \dots, N\}^n$ the corresponding patient IDs, and $y_{\text{test}}^{(\uparrow)} \in \{0, 1\}^n$ the window labels for \uparrow .

Baseline window probabilities. We compute per-window probabilities using the fitted pipeline:

- If the pipeline exposes `predict_proba`, use $\hat{p}^{(\uparrow)} = \text{predict_proba}(X_{\text{test}})[:, 1]$.
- Else if it exposes `decision_function`, map scores to $[0, 1]$ with a sigmoid:

$$\hat{p}^{(\uparrow)} = \sigma(z) = \frac{1}{1 + e^{-z}}.$$

- Else fall back to hard predictions cast to float.

Patient ground truth. Patient-level labels are the OR across that patient's windows:

$$Y_s^{(\uparrow)} = \max_{w \in W_s} y_w^{(\uparrow)}.$$

Patient predictions. We aggregate the window probabilities to patient-level probabilities via p90, then threshold with the already-trained τ_{\uparrow} from the outer training fold:

$$\hat{Y}_s^{(\uparrow)} = \mathbb{1} \left[Q_{0.90}(\{\hat{p}_w^{(\uparrow)}\}_{w \in W_s}) \geq \tau_{\uparrow} \right].$$

Finally, compute the baseline patient-level error $Err_{\text{base}}^{(\uparrow)}$.

A.5.1 Permutation importance: definition and algorithm

For a given feature index j (column j of X_{test}), permutation importance measures how much performance deteriorates when the relationship between that feature and the outcome is broken.

Permutation operator. For one repeat r , we create a perturbed test matrix $X_{\text{test}}^{(j,r)}$ by applying a random permutation π to the rows of feature j :

$$X_{\text{test}}^{(j,r)}[i, j] = X_{\text{test}}[\pi(i), j], X_{\text{test}}^{(j,r)}[i, m] = X_{\text{test}}[i, m] \text{ for } m \neq j.$$

All other features remain unchanged; the marginal distribution of feature j is preserved, but its alignment with labels (and its joint structure with other predictors) is disrupted—thereby testing how much the trained model relies on that feature.

Recompute the full patient-level decision. Using the *same fixed pipeline* and the *same fixed threshold* τ_{\uparrow} , we obtain:

1. window probabilities $\hat{p}_{w,(j,r)}^{(\uparrow)}$ from $X_{\text{test}}^{(j,r)}$,

2. patient-level probabilities by p90,

3. patient-level predictions $\hat{Y}_{s,(j,r)}^{(\uparrow)}$,

4. permuted patient error $Err_{(j,r)}^{(\uparrow)}$.

Importance score. The importance of feature j for label $\hat{\gamma}$ in fold k is defined as the mean increase in patient error rate across repeats:

$$\Delta_j^{(\hat{\gamma})} = \frac{1}{R} \sum_{r=1}^R \left(Err_{(j,r)}^{(\hat{\gamma})} - Err_{\text{base}}^{(\hat{\gamma})} \right),$$

with $R = 5$ repeats, and we also report the standard deviation across repeats as a stability indicator.

Interpretation:

- $\Delta_j^{(\hat{\gamma})} > 0$: permuting feature j increases errors \Rightarrow the feature contributes positively to correct patient-level classification.
- $\Delta_j^{(\hat{\gamma})} \approx 0$: little to no effect \Rightarrow the feature is not used (or its information is redundant).
- $\Delta_j^{(\hat{\gamma})} < 0$: permuting improves error \Rightarrow the feature may be spurious/overfitting for that fold (rare but informative).

A.5.2 Runtime control and consistency with feature selection

To keep the computation tractable and aligned with the fitted pipeline, permutation importance is computed **only on candidate features that are actually available to the classifier**:

- If the pipeline contains SelectKBest, we permute only the subset selected in that fold for that label (retrieved via the selector support mask).
- We additionally cap the number of permuted features to the first $M = 50$ selected features per label per fold (configurable), to avoid quadratic runtime in d .

This is crucial: the importance scores quantify reliance on features **after** the selection stage used during training, not the importance of excluded features.

A.5.3 Aggregation and reporting across folds / models

The procedure yields a long-format importance table with, for each (model configuration, fold, label, feature):

- baseline patient error,
- ΔErr_{mean} and standard deviation across repeats,
- feature identity (name, index),
- fold and model metadata.

Downstream summarization typically reports, for each phenotype, the top-ranked features (largest ΔErr) aggregated across folds (e.g., mean rank or mean ΔErr), and optionally stratified by feature families (statistical/temporal/spectral/complexity) and anatomical segments (landmark channels).

A.5.4 Methodological cautions (important for interpretation)

1. **Correlation and redundancy.** Permutation importance can underestimate a feature's true relevance when strongly correlated predictors exist, because other features can partially compensate after permutation.
2. **Model-conditional nature.** Importance is conditional on the trained model family, pre-processing, and the selected subset of features. It is not an intrinsic property of the raw signal alone.
3. **Patient-level objective.** Because importance is defined on *patient-level error*, it specifically highlights features that affect the final clinical phenotyping decision (post p90 pooling + thresholds), which may differ from what would be most important at the window level.